

Priors with Coupled First and Second Order Differences for Manifold-Valued Image Processing

September 5, 2017

Recently variational models with priors involving first and second order derivatives resp. differences were successfully applied for image restoration. There are several ways to incorporate the derivatives of first and second order into the prior, for example additive coupling or using infimal convolution (IC), as well as the more general model of total generalized variation (TGV). The later two methods give also decompositions of the restored images into image components with distinct “smoothness” properties which are useful in applications.

This paper is the first attempt to generalize these models to manifold-valued images. We propose both extrinsic and intrinsic approaches. The extrinsic approach is based on embedding the manifold into an Euclidean space of higher dimension. Models following this approach can be formulated within the Euclidean space with a constraint restricting them to the manifold. Then alternating direction methods of multipliers can be employed for finding minima. However, the components within the infimal convolution or total generalized variation decomposition live in the embedding space rather than on the manifold which makes their interpretation difficult. Therefore we also investigate two intrinsic approaches. For manifolds which are Lie groups we propose three priors which exploit the group operation, an additive one, another with IC coupling and a third TGV like one. For computing the minimizers of the intrinsic models we apply gradient descent algorithms. For general Riemannian manifolds we further define a model for infimal convolution based on the recently developed second order differences.

*Department of Mathematics, Technische Universität Kaiserslautern, Paul-Ehrlich-Str. 31, 67663 Kaiserslautern, Germany, {bergmann, fitschen, persch, steidl}@mathematik.uni-kl.de.

[†]Fraunhofer ITWM, 67663 Kaiserslautern, Germany

We demonstrate by numerical examples that our approaches works well for the circle, the 2-sphere, the rotation group, and the manifold of positive definite matrices with the affine invariant metric.

1. Introduction

Due to their flexibility to model a large variety of tasks and their efficiency in computing, variational methods have gained a lot of interest in image processing in recent years. Typically, such models are of the form

$$\mathcal{E}(u) = \mathcal{D}(u; f) + \alpha \mathcal{R}(u), \quad \alpha > 0, \quad (1)$$

where f is the given data set, $\mathcal{D}(u; f)$ the data fitting term and $\mathcal{R}(u)$ the regularization term also known as prior. In this paper, we restrict our attention to least squares data fitting terms. Starting with methods having first order derivatives in their prior like the total variation (TV) [44], higher order derivatives were incorporated into the prior to cope with the staircasing effect caused by TV regularization and to better adapt to specific applications. Besides additive coupling of higher order derivatives, see, e.g., [40], their infimal convolution (IC) [24] or the total generalized variation (TGV) [20] were proposed in the literature. In many applications such as image denoising the combination of first and second order differences by IC [45, 46] or TGV [20, 10] shows better results than just the additive coupling.

With the emerging possibilities to capture different modalities of data, image processing methods are transferred to the case where the measurements (pixels) take values on Riemannian manifolds. Examples are Interferometric Synthetic Aperture Radar (InSAR) [12, 23] with values on the circle \mathbb{S}^1 , directional data on the 2-sphere \mathbb{S}^2 , electron backscatter diffraction (EBSD) with data on quotient manifolds of $\text{SO}(3)$ or diffusion tensor magnetic resonance imaging (DT-MRI) [28], where each measurement is a symmetric positive definite 3×3 matrix. These are rather simple manifolds for which explicit expressions of their geodesic distance and exponential map are known.

Recently, the discrete TV regularization has been generalized to Riemannian manifolds in an intrinsic way [38, 49, 53]. Note that finding a global minimizer of the optimization problem is NP hard already for the case of the circle $\mathcal{M} = \mathbb{S}^1$ [25, 27]. In [7, 17, 18] the model was extended to also include second order differences, where the coupling of the differences was realized in an additive manner. The approach is based on a proper generalization of absolute values of second order differences to the manifold-valued setting. For the special case of DT-MRI, i.e., symmetric positive definite matrices of size 3×3 , another approach using tensor calculus resulting in the Frobenius norm instead of a distance on the Riemannian manifold was investigated in [48] and extended to a TGV approach in [51].

In this paper we generalize the discrete variational models with least squares data term and three different priors which combine first and second order derivatives in an additive way, by IC and TGV to the manifold-valued case. We derive extrinsic and intrinsic approaches. The extrinsic models which generalize the first order model in [42, 43]

have the drawback that decompositions of the reconstructed image into the components appearing in the IC or TGV are meaningless, while they may be interpreted as piecewise constant and piecewise “geodesic” parts in the intrinsic approach. For manifolds which are at the same time Lie groups as the special orthogonal group $SO(3)$, differences can be introduced based on the group operation. Together with the geodesic distance notation this leads to the desired models. For more general Riemannian manifolds, our approaches for an additive and an IC prior rely on the generalization of the absolute value of the second order difference by the distance of its center point from a geodesic joining the two other points [7]. For finding a (local) minimizer of the functionals we consider an alternating direction method of multipliers (ADMM) in the extrinsic case. For the intrinsic models we smooth the functionals so that a gradient descent algorithm can be applied. Various numerical examples show the denoising potential of the models in contrast to other approaches. Further, we present a first model for restoring images from EBSD using both the data of the rotation group and the mean angular deviation.

This paper is based on the conference paper [14], where the authors were invited to submit a full journal paper to JMIV.

The outline of the paper is as follows: in the next Section 2 we recall the variational models for denoising gray-values images which we want to generalize. For convenience, we start with the continuous setting and switch to the discrete one afterward. In Section 3 we propose three extrinsic models and show how the ADMM algorithm can be adapted to these models. Then, we focus on intrinsic models in Section 4. We propose two different approaches. The first approach in Subsection 4.1 is restricted to Lie groups and is based on the group operation. The second attempt in Subsection 4.2 works for more general manifolds. It generalizes the priors with additive coupling of first and second order differences to their IC coupling. In Subsection 4.3 we show how minimizers of the (smoothed) intrinsic models can be computed via a gradient descent algorithm. We present numerical examples in Section 5. The paper finishes with conclusions in Section 6.

2. Models for Real-Valued Images

In this section we briefly reconsider models with priors containing first and second order derivatives/differences for gray-value images, where the focus is on the coupling of first and second order terms. To keep the technicalities simple we just rely on gray-value images, but the approach can be simply generalized to images with values in an Euclidean space as, e.g., color RGB images. The modeling for manifold-valued images is based on the discrete models discussed in the second part of this section. However, to get a better intuition on the discrete modeling we start with their background in the continuous setting.

2.1. Continuous Models

We consider images as functions $f: \Omega \rightarrow \mathbb{R}$, where $\Omega \subset \mathbb{R}^2$ is an open, bounded domain with Lipschitz boundary. We restrict our attention to variational models (1) with squared

L_2 data fitting term

$$\mathcal{D}(u; f) := \frac{1}{2} \|f - u\|_{L_2}^2 \quad (2)$$

and discuss several priors. The prior \mathcal{R} contains a priori knowledge on the unknown image. For example, it might reflect that it is smooth or piecewise constant. We focus on the modeling of priors via first and second order derivatives of functions. A frequently applied prior is *total variation* (TV) proposed by Rudin, Osher, and Fatemi [44]. It assumes that the images are in the Banach space of functions with bounded variation $BV(\Omega)$, with norm $\|u\|_{BV} := \|u\|_{L_1} + \text{TV}(u)$, where

$$\text{TV}(u) := \sup_{C_c^\infty(\Omega, \mathbb{R}^2), |\varphi| \leq 1} \int_{\Omega} u \operatorname{div} \varphi \, dx.$$

Here, $C_c^\infty(\Omega, \mathbb{R}^2)$ denotes the space of compactly supported, smooth functions on Ω mapping to \mathbb{R}^2 . The distributional first order derivative Du is a vector-valued Radon measure with total variation $|Du|(\Omega) = \text{TV}(u)$. In particular for $u \in W^{1,1}(\Omega)$, the regularizer becomes

$$\text{TV}(u) = \int_{\Omega} |\nabla u| \, dx. \quad (3)$$

The minimizer of the squared L_2 -TV model preserves edges in images, but prefers piecewise constant solutions, which lead to the so-called stair-casing effect. One possibility to avoid stair-casing effects is to incorporate second order derivatives into the regularizer. To this end we consider the Banach space of functions with *bounded Hessian* $BH(\Omega)$ with norm $\|u\|_{BH} := \|u\|_{BV} + \text{TV}_2(u)$, where

$$\text{TV}_2(u) := \sup_{\substack{\varphi \in C_c^2(\Omega, \mathbb{R}^{2,2}) \\ |\varphi| \leq 1}} \int_{\Omega} u \operatorname{div}^2 \varphi \, dx$$

and

$$\operatorname{div}^2 \varphi := \partial_{xx}\varphi_{11} + \partial_{xy}\varphi_{12} + \partial_{yx}\varphi_{21} + \partial_{yy}\varphi_{22}.$$

If $u \in W^{2,1}(\Omega)$ the term reduces to

$$\text{TV}_2(u) = \int_{\Omega} (u_{xx}^2 + u_{xy}^2 + u_{yx}^2 + u_{yy}^2)^{\frac{1}{2}} \, dx, \quad (4)$$

i.e., we integrate the Frobenius norm of the Hessian of u . Finally, we consider the Banach space $\text{BGV}_\lambda^2(\Omega)$, $\lambda \in \mathbb{R}_{>0}^2$ of *total generalized variation* of order two [20] with norm $\|u\|_{\text{BGV}_\lambda^2} := \|u\|_{L_1} + \text{TGV}_\lambda^2(u)$, where

$$\text{TGV}_\lambda^2(u) := \sup_{\substack{\varphi \in C_c^\infty(\Omega, \text{Sym}(\mathbb{R}^2)), \\ \|\varphi\| \leq \lambda_1, \|\operatorname{div} \varphi\| \leq \lambda_2}} \int_{\Omega} u \operatorname{div}^2 \varphi \, dx.$$

Here $Sym(\mathbb{R}^2)$ denotes the space of symmetric 2×2 matrices, i.e., we have $\varphi_{12} = \varphi_{21}$.

The *infimal convolution* (IC) of two functions $F_i: \mathbb{R}^N \rightarrow \mathbb{R} \cup \{+\infty\}$, $i = 1, 2$, is defined by

$$(F_1 \square F_2)(u) = \inf_{u=v+w} \{F_1(v) + F_2(w)\}.$$

If F_i , $i = 1, 2$, are proper, convex, lower semi-continuous and $F_i(u) = F_i(-u)$, then $F_1 \square F_2$ is also proper, convex, lower semi-continuous and the infimum is attained [41, 46]. A prominent example is the IC of a function F_1 with the squared Euclidean norm, known as Moreau envelope of F_1 . In various applications, the individual IC components v and w are of interest, e.g., in motion separation [36] or crack detection [11]. The IC of the TV functional with other functionals, which are often concatenations of norms and certain linear operators, was used for texture-structure or line-point separation [5, 47, 26].

We consider three common ways to incorporate first and second order information in a prior, namely in an additive way, by IC and by the more sophisticated TGV. The corresponding priors look as follows:

1. **Additive Coupling:**

$$TV_{1 \wedge 2}(u) := \beta TV(u) + (1 - \beta)TV_2(u), \quad \beta \in (0, 1).$$

2. **Infimal Convolution:** The *infimal convolution* (IC) of βTV and $(1 - \beta)TV_2$ is defined by

$$\begin{aligned} IC(u) &:= (\beta TV \square (1 - \beta)TV_2)(u) \\ &= \inf_{u=v+w} \{\beta TV(v) + (1 - \beta)TV_2(w)\}. \end{aligned}$$

3. **Total Generalized Variation:** According to our model (1) we consider TGV_λ with $\lambda := (\beta, 1 - \beta)$. In [21], it was shown that TGV_λ can alternatively be characterized as

$$TGV(u) = \inf_{a \in BD(\Omega, \mathbb{R}^2)} \{\beta |Du - a|(\Omega) + (1 - \beta) |\mathcal{E}a|(\Omega)\},$$

where $BD(\Omega, \mathbb{R}^2)$ is the space of functions with bounded deformation, and $\mathcal{E}a$ is the weak symmetrized derivative of a . Under sufficient smoothness assumptions, the term reduces to

$$TGV(u) = \inf_a \left\{ \beta \int_{\Omega} |\nabla u - a| dx + (1 - \beta) \int_{\Omega} |\tilde{\nabla}a| dx \right\},$$

$$\text{where } |\tilde{\nabla}a| := (a_{1,x}^2 + \frac{1}{2}(a_{1,y} + a_{2,x})^2 + a_{2,y}^2)^{\frac{1}{2}}.$$

2.2. Discrete Models

For the rest of this paper, let

$$\mathcal{G} := \{1, \dots, N_1\} \times \{1, \dots, N_2\}$$

denote the pixel grid of an image of size $N_1 \times N_2$ and let $N := N_1 N_2$. We address grid points by $\mathbf{x} = (x, y)$. Let $u: \mathcal{G} \rightarrow \mathbb{R}$ be a gray-value image. As data fitting term we focus on the the discrete version of (2) given by

$$\mathcal{D}(u; f) = \frac{1}{2} \|f - u\|_2^2. \quad (5)$$

To set up the different priors we need a careful discretization of the involved differential operators. By $\nabla_x f$ we denote the forward differences in x -direction with Neumann boundary conditions

$$(\nabla_x u)_{\mathbf{x}} := \begin{cases} u_{\mathbf{x}+(1,0)} - u_{\mathbf{x}} & \text{if } \mathbf{x} + (1, 0) \in \mathcal{G}, \\ 0 & \text{otherwise,} \end{cases}$$

and by $\tilde{\nabla}_x u$ the backward differences in x -direction

$$(\tilde{\nabla}_x u)_{\mathbf{x}} = \begin{cases} u_{\mathbf{x}} - u_{\mathbf{x}-(1,0)} & \text{if } \mathbf{x} \pm (1, 0) \in \mathcal{G}, \\ 0 & \text{otherwise.} \end{cases}$$

The zero at the right boundary of the backward difference is chosen due to (10). By definition of the forward difference, the first summand in (10) enforces the last term of a_i , $i = 1, 2$, to become zero and this should not influence the other terms of a by an appropriate definition of $\tilde{\nabla}$ in the second summand of (10). Differences in y -direction are defined analogously. Then

$$\nabla := \begin{pmatrix} \nabla_x \\ \nabla_y \end{pmatrix}$$

serves as discrete gradient and we can define

$$\Delta_x := \tilde{\nabla}_x \nabla_x, \quad (6)$$

i.e.,

$$(\Delta_x u)_{\mathbf{x}} = \begin{cases} u_{\mathbf{x}-(1,0)} - 2u_{\mathbf{x}} + u_{\mathbf{x}+(1,0)} & \text{if } \mathbf{x} \pm (1, 0) \in \mathcal{G}, \\ 0 & \text{otherwise.} \end{cases}$$

To use terms of the Hessian, we introduce mixed second order differences

$$D_{xy} = \tilde{\nabla}_y \nabla_x \quad (7)$$

and analogously for the other directions. Then, using

$$\tilde{\nabla} := \begin{pmatrix} \tilde{\nabla}_x & \\ \frac{1}{2} \tilde{\nabla}_y & \frac{1}{2} \tilde{\nabla}_x \\ & \tilde{\nabla}_y \end{pmatrix},$$

we can define the *symmetrized Hessian* as

$$\nabla^2 := \tilde{\nabla} \nabla = \begin{pmatrix} \Delta_x \\ \frac{1}{2}(D_{xy} + D_{yx}) \\ \Delta_y \end{pmatrix}. \quad (8)$$

For details on the discretization in particular for TGV we refer to [46]. Finally, we introduce a mixed norm for $v: \mathcal{G} \rightarrow \mathbb{R}^d$ by

$$\|\cdot\|_{r,s}^s := \sum_{\mathbf{x} \in \mathcal{G}} \|v_{\mathbf{x}}\|_r^s, \quad \|v_{\mathbf{x}}\|_r^r := \sum_{k=1}^d v_{\mathbf{x},k}^r \quad r, s \geq 1.$$

Then the discrete TV regularizer (3) is given by

$$\begin{aligned} \text{TV}(u) &= \|\nabla u\|_{2,1} \\ &= \sum_{\mathbf{x} \in \mathcal{G}} \left(\sum_{\mathbf{y} \in \mathcal{N}_{\mathbf{x}}} |u_{\mathbf{y}} - u_{\mathbf{x}}|^2 \right)^{\frac{1}{2}}, \end{aligned} \quad (9)$$

where $\mathcal{N}_{\mathbf{x}} := \{\mathbf{x} + (0, 1), \mathbf{x} + (1, 0)\} \cap \mathcal{G}$ denotes the forward neighbors. For the TV_2 regularizer (4) we use also the symmetrized Hessian (8) which leads to

$$\begin{aligned} \text{TV}_2(u) &= \|\nabla^2 u\|_{2,1} \\ &= \sum_{\mathbf{x} \in \mathcal{G}} \left(|(\Delta_x u)_{\mathbf{x}}|^2 + |(\Delta_y u)_{\mathbf{x}}|^2 + \frac{1}{4} ((D_{xy} u)_{\mathbf{x}} + (D_{yx} u)_{\mathbf{x}})^2 \right)^{\frac{1}{2}}. \end{aligned}$$

Now the three discrete priors read as follows:

1. **Additive Coupling:**

$$\text{TV}_{1\wedge 2}(u) = \beta \|\nabla u\|_{2,1} + (1 - \beta) \|\nabla^2 u\|_{2,1}.$$

2. **Infimal Convolution:**

$$\begin{aligned} \text{IC}(u) &= \min_{u=v+w} \{ \beta \|\nabla v\|_{2,1} + (1 - \beta) \|\nabla^2 w\|_{2,1} \} \\ &= \min_w \{ \beta \|\nabla(u - w)\|_{2,1} + (1 - \beta) \|\nabla^2 w\|_{2,1} \}. \end{aligned}$$

3. **Total Generalized Variation:**

$$\text{TGV}(u) = \min_a \left\{ \beta \|\nabla u - a\|_{2,1} + (1 - \beta) \|\tilde{\nabla} a\|_{2,1} \right\}. \quad (10)$$

In case a can be written as $a = \nabla w$ for some $w: \mathcal{G} \rightarrow \mathcal{R}$, i.e., a is a conservative vector field, we get $\tilde{\nabla} a = \tilde{\nabla} \nabla w = \nabla^2 w$. In this case the TGV model coincides with the IC one. While the TGV model is in this sense more general than the decomposition used by IC, it further does not require the computation of second order differences. In [10] the model and in particular the involved decomposition was successfully applied to motion vector fields for the early detection of cracks in materials during tensile tests.

3. Extrinsic Models for Manifold-Valued Images

To introduce manifold-valued images, we have to exchange the real- or vector-valued range space from the previous section by a manifold. Let \mathcal{M} be a connected, simply-connected, complete d -dimensional Riemannian manifold. By $T_p\mathcal{M}$ we denote the tangent space of \mathcal{M} at $p \in \mathcal{M}$ with the Riemannian metric $\langle \cdot, \cdot \rangle_p$. Let $\gamma_{p,q}$ be a (not necessarily shortest) geodesic connecting $p, q \in \mathcal{M}$ and $\text{dist}: \mathcal{M} \times \mathcal{M} \rightarrow \mathbb{R}_{\geq 0}$ the geodesic distance on \mathcal{M} . By \mathcal{M}^N we denote the product or N -fold power manifold with usual product distance.

Instead of gray-value images, we consider images $u: \mathcal{G} \rightarrow \mathcal{M}$ with values on a manifold. In our numerical experiments with extrinsic and intrinsic models we deal with the following manifolds:

- spheres \mathbb{S}^d , $d = 1, 2$, which includes the important case of cyclic (phase) data;
- special orthogonal group $\text{SO}(3)$;
- symmetric positive definite $r \times r$ matrices $\mathcal{P}(r)$.

The explicit expressions required for our computations are given in the Appendix B. The first two kind of manifolds are compact, while $\mathcal{P}(r)$ is an open convex cone in $\mathbb{R}^{r,r}$.

The simplest idea to generalize the models from the previous section to manifold-valued images is to embed the manifold into the Euclidean space and to apply the Euclidean models with the constraint that the image values have to lie in a manifold. To express the manifold constrained we use the indicator function of a set S defined by

$$\iota_S(u) := \begin{cases} 0 & \text{if } u \in S, \\ +\infty & \text{otherwise.} \end{cases}$$

Recall that by Whitney's theorem [54] every smooth d -dimensional manifold can be smoothly embedded into an Euclidean space of dimension $n = 2d$. Moreover, by Nash's theorem [39] every Riemannian manifold can be isometrically embedded into an Euclidean space of suitable dimension. For the squared L_2 -TV model such an approach was given in [42, 43] with a sketch how it can be generalized for an additive model with first and second order differences similar to the one considered below.

Here are our three models, where we assume that \mathcal{M} is embedded in \mathbb{R}^n and we minimize over $u \in \mathbb{R}^{nN}$.

1. Additive Coupling:

$$E_{\text{Add}}^{\text{ext}}(u) := \frac{1}{2} \|f - u\|_2^2 + \alpha \text{TV}_{1 \wedge 2}(u) + \iota_{\mathcal{M}^N}(u).$$

2. Infimal Convolution:

$$E_{\text{IC}}^{\text{ext}}(u) := \frac{1}{2} \|f - u\|_2^2 + \alpha \text{IC}(u) + \iota_{\mathcal{M}^N}(u)$$

We directly want to compute the components v, w , i.e., we are searching for minimizers $v, w \in \mathbb{R}^{nN}$ of

$$\begin{aligned}\mathcal{E}_{\text{IC}}^{\text{ext}}(v, w) := & \frac{1}{2} \|f - v - w\|_2^2 + \iota_{\mathcal{M}^N}(v + w) \\ & + \alpha(\beta \text{TV}(v) + (1 - \beta) \text{TV}_2(w))\end{aligned}\tag{11}$$

and set finally $u := v + w$.

3. Total Generalized Variation:

$$E_{\text{TGV}}^{\text{ext}}(u) := \frac{1}{2} \|f - u\|_2^2 + \alpha \text{TGV}(u) + \iota_{\mathcal{M}^N}(u)$$

More precisely we are looking for the minimizer of

$$\begin{aligned}\mathcal{E}_{\text{TGV}}^{\text{ext}}(u, a) := & \frac{1}{2} \|f - u\|_2^2 + \iota_{\mathcal{M}^N}(u) \\ & + \alpha \left(\beta \|\nabla u - a\|_{2,1} + (1 - \beta) \|\tilde{\nabla} a\|_{2,1} \right)\end{aligned}$$

If \mathcal{M} is closed, we directly get the existence of a global minimizer by the coercivity and lower semi-continuity of the functional.

As also suggested in [42, 43], we apply an alternating direction method of multipliers (ADMM) to minimize the above functionals. The ADMM dates back to [29, 33] and a frequently cited paper on recent applications is [19]. We give the general algorithm in the form detailed in [22] and show how it can be specified for our three settings: Intending to find a minimizer of

$$E(x) := g(x) + H(Ax) = g(x) + \sum_{i=1}^d h_i(A_i x)$$

with a linear operator A , we rewrite the task by splitting the functional as

$$\mathcal{E}(x, y) := g(x) + H(y) = g(x) + \sum_{i=1}^d h_i(y_i) \quad \text{subject to} \quad Ax = y,$$

where $y = (y_1, \dots, y_d)^T$. Based on the augmented Lagrangian

$$L_\gamma(x, y, b) := g(x) + H(y) + \frac{\gamma}{2} \|Ax - y + b\|_2^2$$

the ADMM alternates the minimization of the augmented Lagrangian in x, y and updates of the Lagrangian multiplier b as outlined in Algorithm 1.

Algorithm 1 ADMM

Input: f, A
Initialization: $y^{(0)} = b^{(0)}$,

for $r = 0, \dots$ **do**

$$x^{(r+1)} = \arg \min_x \left\{ \frac{1}{2} \|x - f\|_2^2 + \frac{\gamma}{2} \|Ax - y^{(r)} + \frac{1}{\gamma} b^{(r)}\|_2^2 \right\}$$

for $i = 1, \dots, d$ **do**

$$y_i^{(r+1)} = \arg \min_{y_i} \left\{ h_i(y_i) + \frac{\gamma}{2} \|A_i x^{(r+1)} - y_i + \frac{1}{\gamma} b_i^{(r)}\|_2^2 \right\}$$

$$b^{(r+1)} = b^{(r)} + \gamma(Ax^{(r+1)} - y^{(r+1)})$$

In our models we apply the algorithm with

$$\begin{aligned} x_{1\wedge 2} &= u, & A_{1\wedge 2} &= \begin{pmatrix} \nabla \\ \nabla^2 \\ I_{nN} \end{pmatrix}, \\ x_{\text{IC}} &= \begin{pmatrix} v \\ w \end{pmatrix}, & A_{\text{IC}} &= \begin{pmatrix} \nabla & \mathbf{0} \\ \mathbf{0} & \Delta \\ I_{nN} & I_{nN} \end{pmatrix}, \\ x_{\text{TGV}} &= \begin{pmatrix} u \\ a \end{pmatrix}, & A_{\text{TGV}} &= \begin{pmatrix} \nabla & -I_{2nN} \\ \mathbf{0} & \tilde{\nabla} \\ I_{nN} & \mathbf{0} \end{pmatrix}, \end{aligned}$$

and $h_1 := \|\cdot\|_{2,1}$ for vector fields $v: \mathcal{G} \rightarrow \mathbb{R}^{2n}$, $h_2 := \|\cdot\|_{2,1}$ for $v: \mathcal{G} \rightarrow \mathbb{R}^{3n}$, and $h_3 := \iota_{\mathcal{M}^N}$. The linear operators can be considered as matrices here.

The first step of Algorithm 1 requires simply the solution of a least squares problem. The next two steps for minimizing the so-called proximum of h_i , $i = 1, 2$ are applications of a grouped soft shrinkage operator with threshold γ to the given data in the squared ℓ_2 -term, see, e.g. [22]. The minimization of the proximum of the indicator function h_3 requires the orthogonal projections onto the manifold. For the spheres $\mathbb{S}^d \subset \mathbb{R}^{d+1}$, this can be realized by just normalizing the vector with respect to the Euclidean norm in \mathbb{R}^{d+1} . For $\text{SO}(3)$, the authors of [42, 43] suggest to embed the $\text{SO}(3)$ into \mathbb{R}^9 . Then the projection requires the singular value decomposition of the matrix in $\mathbb{R}^{3,3}$ we want to project. In this paper, we prefer an embedding of $\text{SO}(3)$ into \mathbb{R}^4 via the quaternion representation, see Appendix B. This reduces the dimension of the problem and the projection is again just a normalization. Finally, $\mathcal{P}(r)$ can be embedded into \mathbb{R}^n , $n = \frac{r(r+1)}{2}$. However, since the manifold is an open subset of \mathbb{R}^n , the approach is not possible

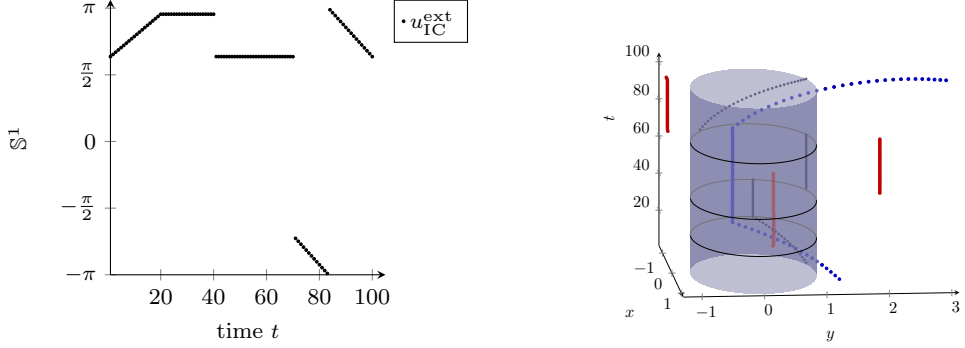


Figure 1 Decomposition of an \mathbb{S}^1 -valued signal $f = u_{\text{IC}}^{\text{ext}}$ (top) by the extrinsic IC approach (11) with $\alpha = 0.03$, $\beta = \frac{1}{3}$. Left: Original piecewise geodesic signal $f = u_{\text{IC}}^{\text{ext}}$ (black) determined by its angles in $[-\pi, \pi]$. Since the decomposition into $v_{\text{IC}}^{\text{ext}}, w_{\text{IC}}^{\text{ext}}$ is within the embedding space \mathbb{R}^3 , they can not be shown or interpreted as elements of \mathbb{S}^1 . Right: Result of the extrinsic IC model with respect to the embedding $\mathbb{S}^1 \subset \mathbb{R}^2$; original signal $u_{\text{IC}}^{\text{ext}}$ (black), its piecewise constant component $v_{\text{IC}}^{\text{ext}}$ (red) and its piecewise linear component $w_{\text{IC}}^{\text{ext}}$ (blue).

in the present form if the iterates do not stay within the manifold itself. A numerical remedy would be to project onto the closed cone and add a small parameter to the eigenvalues of the resulting matrix to make it positive definite. In this paper, we apply only an intrinsic approach to images with values in $\mathcal{P}(r)$.

Concerning the convergence of the ADMM algorithm we mention the following. If \mathcal{M} is a closed, convex set in \mathbb{R}^n , then the algorithm converges by standard arguments. This is the case for (the closure of) $\mathcal{P}(r)$.

For spheres and the $\text{SO}(3)$, convergence is observed numerically but cannot be guaranteed theoretically.

Note that the convergence of the ADMM for special non-convex functionals was recently addressed in [52]. Unfortunately, the assumptions of that paper do not fit into our setting: More precisely, Assumption 2 in [52] would require with respect to our setting that the range of $\begin{pmatrix} \nabla \\ I \end{pmatrix}$ is a subset of the range of the identity matrix which is clearly not the case.

A possibility to circumvent theoretical convergence problems would be to consider a smoothed version of the functional as we do it in (18). Then the functional is Lipschitz differentiable and a gradient projection algorithm can be applied. For such an algorithm convergence was shown in [4] for functions satisfying a Kurdyka-Łojasiewicz property which is fulfilled in most cases. However, such algorithm shows a bad convergence behavior numerically such that we prefer the ADMM.

Example 3.1 We consider the phase-valued (noise-free) signal $f = u_{\text{IC}}^{\text{ext}}$ of length $N_1 = 100$ in the left plot of Fig. 1. It consists of a linearly increasing line, two constant parts divided by a small jump and a decreasing part. The second „jump“ in the signal is smaller than it occurs, since the shorter arc on the circle is the one “wrapping” around

(going over $\pm\pi$). Furthermore, the “jump” at $t = 82$ is just due to the representation system (the choice of the angle zero). We are interested in its decomposition by the extrinsic IC model (11). Embedding each pixel $f_i \in \mathbb{S}^1$ into \mathbb{R}^2 yields a signal in \mathbb{R}^3 shown in the left of Fig. 1 in black. Since the extrinsic model decomposes $u_{\text{IC}}^{\text{ext}}$ within the embedding space \mathbb{R}^2 , both the first order differences part $v_{\text{IC}}^{\text{ext}}$ (red) and the second order difference part $w_{\text{IC}}^{\text{ext}}$ (blue) can only be visualized within \mathbb{R}^3 , in particular not in the right plot. They can not be interpreted as phase-valued data. Still, $v_{\text{IC}}^{\text{ext}}$ is piecewise constant and contains the jumps, and $w_{\text{IC}}^{\text{ext}}$ is continuous.

4. Intrinsic Models for Manifold-Valued Images

In this section, we develop intrinsic variational models to process manifold-valued images $u: \mathcal{G} \rightarrow \mathcal{M}$. Indeed the generalization of first order models is rather straightforward. Instead of the data term (5) we use

$$\mathcal{D}(u; f) = \frac{1}{2} \sum_{\mathbf{x} \in \mathcal{G}} \text{dist}^2(f_{\mathbf{x}}, u_{\mathbf{x}}) = \frac{1}{2} \mathbf{dist}^2(f, u),$$

where **dist** denotes the distance on the product manifold \mathcal{M}^N . We define the TV term for manifold-valued images by replacing the absolute differences in (9) by distances on the manifold

$$\text{TV}(u) := \sum_{\mathbf{x} \in \mathcal{G}} \left(\sum_{\mathbf{y} \in \mathcal{N}_{\mathbf{x}}} \text{dist}^2(u_{\mathbf{x}}, u_{\mathbf{y}}) \right)^{\frac{1}{2}}. \quad (12)$$

The model $\mathcal{D}(u; f) + \alpha \text{TV}(u)$ with the above terms was already considered in [38, 53].

In the Euclidean setting, tools from convex analysis can be applied for finding a minimizer of the squared L_2 -TV functional including powerful algorithms based on duality theory as for instance the ADMM used in the previous section. Recently, several attempts have been made to translate concepts from convex analysis to the manifold-valued setting and it turns out that a rich theory of convex functions can be built in so-called Hadamard manifolds, for an overview see, e.g., [6]. These are simply connected, complete Riemannian manifolds of nonpositive sectional curvature, as for example the manifold of positive definite matrices or hyperbolic spaces. In particular, for Hadamard manifolds the squared L_2 -TV functional is convex so that several algorithms as, e.g., the cyclic proximal point algorithm can be proved to converge, see [53].

To incorporate second order differences in the functional for the manifold-valued setting is not straightforward. First of all there is no general definition of second order differences for manifold-valued data. We emphasize that we do not speak about Hessians of functions living on a manifold. In our case the derivatives/differences are in Ω/\mathcal{G} . If the manifold is in particular a Lie group, additions can be replaced by the group operation. We show that a certain generalization of the three models is possible in the next subsection. Then we turn to general manifold. Here we adopt the definition of the absolute value of second order differences from [7]. This basic approach can be

also applied for defining so-called midpoint infimal convolutions and a corresponding IC model.

4.1. Intrinsic Models for Lie Group-Valued Images

Let us assume that the manifold \mathcal{M} is in addition a Lie group with group action $\circ: \mathcal{M} \times \mathcal{M} \rightarrow \mathcal{M}$ and unit element $e \in \mathcal{M}$. This means that the group action as well as the mapping $p \mapsto p^{-1}$, $p \in \mathcal{M}$ are smooth. Our focus is on matrix Lie groups, where the identity $e = I$. Examples are the sphere \mathbb{S}^1 and $\text{SO}(3)$. The *left* and *right translation* $L_p, R_p: \mathcal{M} \times \mathcal{M} \rightarrow \mathcal{M}$ with respect to $p \in \mathcal{M}$ are given by

$$L_p(q) := p \circ q, \quad R_p(q) := q \circ p,$$

respectively. A metric of a Lie group is called *left*-, resp. *right-invariant* if for all $p, q \in \mathcal{M}$ and all $\xi, \nu \in T_q \mathcal{M}$ it holds

$$\begin{aligned} \langle \xi, \nu \rangle_q &= \langle DL_p(q)[\xi], DL_p(q)[\nu] \rangle_{p \circ q}, \quad \text{resp.} \\ \langle \xi, \nu \rangle_v &= \langle DR_p(q)[\xi], DR_p(q)[\nu] \rangle_{q \circ p}. \end{aligned}$$

Therefore a left (right) invariant metric is induced by a metric on the tangent space $T_e \mathcal{M}$ which is actually the Lie algebra of \mathcal{M} . A left- and right-invariant metric on a Lie group is called bi-invariant. For matrix groups we will use the Frobenius inner product on $T_e \mathcal{M}$. Every compact Lie group, in particular \mathbb{S}^1 and $\text{SO}(3)$, admit a bi-invariant metric. Note that certain Lie groups do not have a bi-invariant metric. For example, an elegant proof of the fact that the group of Euclidean transformations $\text{SE}(n)$, $n \geq 2$, does not admit any bi-invariant metric given in [3]. For the distance function on \mathcal{M} equipped with a left resp. right-invariant metric we have

$$\begin{aligned} \text{dist}(p, q) &= \text{dist}(p^{-1} \circ q, e) = \text{dist}(q^{-1} \circ p, e), \quad \text{resp.} \\ \text{dist}(p, q) &= \text{dist}(p \circ q^{-1}, e) = \text{dist}(e, q \circ p^{-1}). \end{aligned}$$

Next we define the difference operators by replacing additions/subtractions by the group operation where we have to be careful if the group operation is non commutative. Let us suppose that \mathcal{M} has a right-invariant metric. For $\mathbf{x} \in \mathcal{G}$, we define the forward “differences” in x -direction by

$$(\nabla_x u)_{\mathbf{x}} := \begin{cases} u_{\mathbf{x}+(1,0)} \circ u_{\mathbf{x}}^{-1} & \text{if } \mathbf{x} + (1,0) \in \mathcal{G}, \\ e & \text{otherwise} \end{cases}$$

and similarly in y -direction which gives ∇^{Lie} . This fits to the definition of manifold-valued TV since (12) can be rewritten as

$$\text{TV}(u) = \sum_{\mathbf{x} \in \mathcal{G}} \left(\text{dist}^2 ((\nabla_x u)_{\mathbf{x}}, e) + \text{dist}^2 ((\nabla_y u)_{\mathbf{x}}, e) \right)^{\frac{1}{2}}.$$

Similarly, we introduce the backward difference in x -direction by

$$(\tilde{\nabla}_x u)_{\mathbf{x}} = \begin{cases} u_{\mathbf{x}} \circ u_{\mathbf{x}-(1,0)}^{-1} & \text{if } \mathbf{x} \pm (1,0) \in \mathcal{G}, \\ e & \text{otherwise.} \end{cases}$$

Then the operators Δ_x and D_{xy} are given by concatenation as in (6) and (7), respectively. We obtain

$$(\Delta_x u)_{\mathbf{x}} = \begin{cases} u_{\mathbf{x}+(1,0)} \circ u_{\mathbf{x}}^{-1} \circ u_{\mathbf{x}-(1,0)} \circ u_{\mathbf{x}}^{-1} & \text{if } \mathbf{x} \pm (1,0) \in \mathcal{G}, \\ e & \text{otherwise} \end{cases}$$

and

$$(D_{xy} u)_{\mathbf{x}} = (\tilde{\nabla}_y \nabla_x u)_{\mathbf{x}} = \begin{cases} u_{\mathbf{x}+(1,0)} \circ u_{\mathbf{x}}^{-1} \circ u_{\mathbf{x}-(0,1)} \circ u_{\mathbf{x}+(1,-1)}^{-1} & \text{if } \mathbf{x} \pm (0,1) \wedge \\ & \mathbf{x} + (1,0) \in \mathcal{G}, \\ e & \text{otherwise} \end{cases}$$

and use furthermore

$$\tilde{\nabla}^{\text{Lie}} := \begin{pmatrix} \tilde{\nabla}_x & & \\ & \tilde{\nabla}_y & \\ & & \tilde{\nabla}_x \\ & & & \tilde{\nabla}_y \end{pmatrix}.$$

Similar to the norm $\|\cdot\|_{r,s}$ on vector fields we define the $\text{dist}_{r,s}$ for $a, b: \mathcal{G} \rightarrow \mathcal{M}^d$ as

$$\text{dist}_{r,s}^s(a, b) = \sum_{\mathbf{x} \in \mathcal{G}} \left(\sum_{i=1}^d \text{dist}^r(a_{\mathbf{x},i}, b_{\mathbf{x},i}) \right)^{\frac{s}{r}}.$$

Finally, we set

$$\begin{aligned} (\text{d}_{2,xx}^{\text{Lie}} u)_{\mathbf{x}} &:= \text{dist}((\Delta_x u)_{\mathbf{x}}, e), \\ (\text{d}_{2,yy}^{\text{Lie}} u)_{\mathbf{x}} &:= \text{dist}((\Delta_y u)_{\mathbf{x}}, e), \\ (\text{d}_{2,xy}^{\text{Lie}} u)_{\mathbf{x}} &:= \text{dist}((D_{xy} u)_{\mathbf{x}}, e), \\ (\text{d}_{2,yx}^{\text{Lie}} u)_{\mathbf{x}} &:= \text{dist}((D_{yx} u)_{\mathbf{x}}, e), \end{aligned}$$

and

$$\text{TV}_2^{\text{Lie}} := \sum_{\mathbf{x} \in \mathcal{G}} \left((\text{d}_{2,xx}^{\text{Lie}} u)_{\mathbf{x}}^2 + (\text{d}_{2,yy}^{\text{Lie}} u)_{\mathbf{x}}^2 + \frac{1}{2} ((\text{d}_{2,xy}^{\text{Lie}} u)_{\mathbf{x}}^2 + (\text{d}_{2,yx}^{\text{Lie}} u)_{\mathbf{x}}^2) \right)^{\frac{1}{2}}.$$

We can now define the three priors on Lie groups as follows. Note that despite modifications in the coupling of the mixed “difference” we use the same names as before.

1. Additive Coupling:

$$\begin{aligned} \mathcal{E}_{\text{Add}}^{\text{Lie}}(u) &:= \frac{1}{2} \mathbf{dist}^2(f, u) \\ &+ \alpha (\beta \text{TV}(u) + (1 - \beta) \text{TV}_2^{\text{Lie}}(u)) \end{aligned}$$

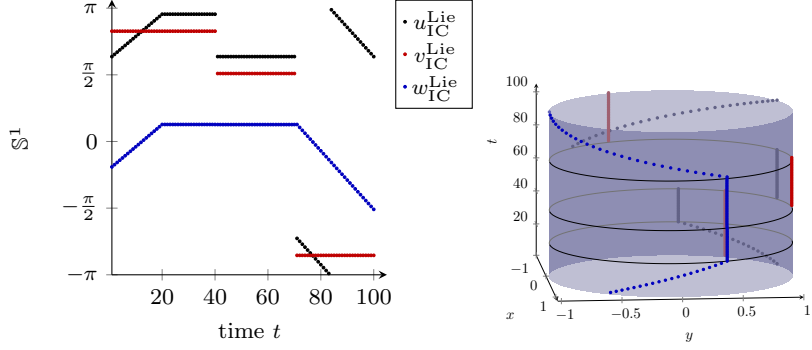


Figure 2 Decomposition of the \mathbb{S}^1 -valued signal $f = u_{\text{IC}}^{\text{Lie}}$ from Fig. 1 by the intrinsic Lie group IC approach (13) ($\alpha = 0.001$, $\beta = \frac{2}{3}$). Left: Original piecewise geodesic signal $u_{\text{IC}}^{\text{Lie}}$ (black) determined by its angles in $[-\pi, \pi]$, the piecewise constant component $v_{\text{IC}}^{\text{Lie}}$ (red), and piecewise geodesic component $w_{\text{IC}}^{\text{Lie}}$ (blue). Right: Result of the intrinsic Lie group IC model in the embedding space \mathbb{R}^2 .

2. Infimal Convolution: The addition in the IC is replaced by the group operation.

$$\begin{aligned} E_{\text{IC}}^{\text{Lie}}(u) := & \frac{1}{2} \mathbf{dist}^2(f, u) \\ & + \alpha \inf_{u=v \circ w} (\beta \text{TV}(v) + (1 - \beta) \text{TV}_2^{\text{Lie}}(w)). \end{aligned}$$

As before we minimize

$$\begin{aligned} \mathcal{E}_{\text{IC}}^{\text{Lie}}(v, w) := & \frac{1}{2} \mathbf{dist}^2(f, v \circ w) \\ & + \alpha (\beta \text{TV}(v) + (1 - \beta) \text{TV}_2^{\text{Lie}}(w)) \end{aligned} \quad (13)$$

with respect to $v, w: \mathcal{G} \rightarrow \mathcal{M}$ and then set $u = v \circ w$.

3. Total Generalized Variation:

$$\begin{aligned} E_{\text{TGV}}^{\text{Lie}}(u) := & \frac{1}{2} \mathbf{dist}^2(f, u) + \alpha \inf_a (\beta \text{dist}_{2,1}(\nabla^{\text{Lie}} u, a) \\ & + (1 - \beta) \text{dist}_{2,1}(\tilde{\nabla}^{\text{Lie}} a, e)) \end{aligned} \quad (14)$$

Here we minimize

$$\begin{aligned} \mathcal{E}_{\text{TGV}}^{\text{Lie}}(u, a) := & \frac{1}{2} \mathbf{dist}^2(f, u) + \alpha \beta \text{dist}_{2,1}(\nabla^{\text{Lie}} u, a) \\ & + \alpha (1 - \beta) \text{dist}_{2,1}(\tilde{\nabla}^{\text{Lie}} a, e) \end{aligned}$$

To find a (local) minimizer of the functionals we will apply a gradient descent algorithm described in Subsection 4.3.

Example 4.1 We continue Example 3.1 and consider the same phase-valued signal $f = u_{\text{IC}}^{\text{Lie}}$ as in Fig. 1. Since $\mathcal{M} = \mathbb{S}^1$ is also a Lie group, we can apply the IC Lie model (13).

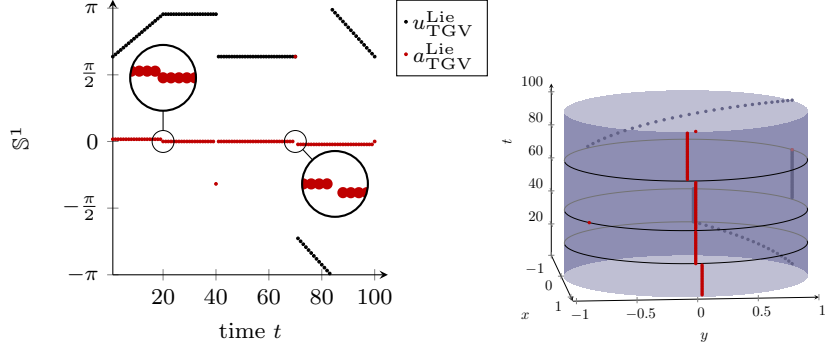


Figure 3 Decomposition of the \mathbb{S}^1 -valued signal from Fig. 1 by the intrinsic Lie group TGV approach (14) ($\alpha = 0.0101$, $\beta = \frac{1}{101}$). Left: Original piecewise geodesic signal $f = u_{\text{TGV}}^{\text{Lie}}$ (black) determined by its angles in $[-\pi, \pi]$ and the compensator $a_{\text{TGV}}^{\text{Lie}}$ (red), which equals the finite differences in this case. Right: Result of the intrinsic Lie group TGV model in the embedding space \mathbb{R}^2 .

Both the first order part v_{IC}^{Lie} and the second order component w_{IC}^{Lie} live on the manifold, so that they can be parametrized in $[-\pi, \pi]$ and plotted within the left plot. The plot in the embedding on the right side is just given for reference to the previous example of the extrinsic model. Again, as expected, the piecewise constant part v_{IC}^{Lie} contains the jumps and the second order component w_{IC}^{Lie} does not contain jumps and is piecewise geodesic.

Example 4.2 We continue the Examples 3.1 and 4.1 and apply the TGV Lie model (14) to the signal $f = u_{\text{TGV}}^{\text{Lie}}$ explained in the examples before. Since we are concerned with a signal, the component $a_{\text{TGV}}^{\text{Lie}}$ from the TGV model approximates the (discrete) gradient, i.e. the finite differences of f . The resulting $a_{\text{TGV}}^{\text{Lie}}$ is shown in Fig. 3 (red). In the first linear increasing part the approximated gradient is constant and positive, in the last part it is constant, negative with larger absolute value than for the first part due to the steeper descent in the last interval. For the two constant parts, $a_{\text{TGV}}^{\text{Lie}}$ is zero, and at the jump positions one can observe an outlier indicating the jump height and direction.

4.2. Intrinsic Models Using a Mid Point Formulation

To establish models for images $f : \mathcal{G} \rightarrow \mathcal{M}$ with data in more general manifolds we have to propose a definition of the absolute value of second order differences. Observing that in the Euclidean case the second order difference of $x_1, x_1, x_3 \in \mathbb{R}^d$ can be rewritten as $|x_1 - 2x_2 + x_3| = 2|\frac{1}{2}(x_1 + x_3) - x_2|$, we define a counterpart for $p_1, p_2, p_3 \in \mathcal{M}$ as follows [7]: let \mathcal{C}_{p_1, p_3} be the set of mid points $\gamma_{p_1, p_3}(\frac{1}{2})$ of all geodesics joining p_1 and p_3 . Then we define the *second order finite difference* as

$$d_2(p_1, p_2, p_3) := \min_{c \in \mathcal{C}_{p_1, p_3}} \text{dist}(c, p_2).$$

For an illustration see Fig. 4. Note that the geodesic γ_{p_1, p_3} is unique on manifolds with non positive curvature, i.e., on Hadamard manifolds. This technique can further be

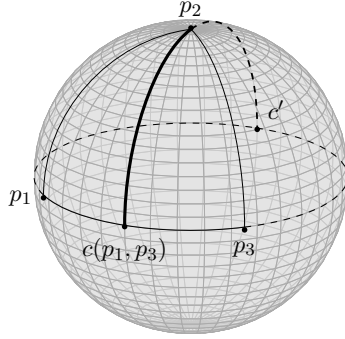


Figure 4 Illustration of the absolute second order difference on the sphere \mathbb{S}^2 given by the length of the line connecting p_2 and its nearest mid point $c(x, z) \in \mathcal{C}_{p_1, p_3}$. Nevertheless on \mathbb{S}^2 there is a second candidate $c' \in \mathcal{C}_{p_1, p_3}$, which is the mid point of the longer arc of the great circle defined by p_1 and p_3 .

employed to define the *second order mixed difference* [18] for $p_i \in \mathcal{M}, i = 1, \dots, 4$, as

$$d_{1,1}(p_1, p_2, p_3, p_4) := \min_{c \in \mathcal{C}_{p_1, p_3}, \tilde{c} \in \mathcal{C}_{p_2, p_4}} \text{dist}(c, \tilde{c}).$$

Remark 4.3 Note that for Hadamard manifolds, in contrast to the distance function employed in the TV functional, the second order absolute difference d_2 is neither convex in p_1 nor in p_3 .

Using this definition we introduce the absolute value of the second order difference in x -direction as counterpart of the Euclidean $\frac{1}{2}|\Delta_x(u)_x|$ by

$$(d_{2,xx}^{\text{int}} u)_x := \begin{cases} d_2(u_{x+(1,0)}, u_x, u_{x-(1,0)}) & \text{if } x \pm (1,0) \in \mathcal{G}, \\ 0 & \text{otherwise} \end{cases}$$

and similarly in y -direction. For the absolute values of the mixed derivatives $|(D_{xy}u)_x|$ we use

$$(d_{2,xy}^{\text{int}} u)_x := \begin{cases} d_{1,1}(u_x, u_{x+(0,-1)}, u_{x+(1,0)}, u_{x+(1,-1)}) & \text{if } x \pm (0,1) \wedge x + (1,0) \in \mathcal{G}, \\ 0 & \text{otherwise,} \end{cases}$$

and similarly with interchanged roles of forward and backward differences $d_{2,yx}^{\text{int}} u$. Then we define the (isotropic) second order total variation term by

$$\text{TV}_2^{\text{int}}(u) := \sum_{x \in \mathcal{G}} \left((d_{2,xx}^{\text{int}} u)_x^2 + (d_{2,yy}^{\text{int}} u)_x^2 + \frac{1}{2} ((d_{2,xy}^{\text{int}} u)_x^2 + (d_{2,yx}^{\text{int}} u)_x^2) \right)^{\frac{1}{2}}.$$

To set up our IC model we realize that in the Euclidean setting the IC of two one-homogeneous functions as TV and TV_2 can be rewritten as

$$F_1 \square F_2(u) = \frac{1}{2} \inf_{u=\frac{1}{2}(v+w)} \{F_1(v) + F_2(w)\}.$$

Now we may consider the “midpoint infimal convolution” of $F_i: \mathcal{M} \rightarrow \mathbb{R}$, $i = 1, 2$, given by

$$F_1 \square_m F_2(u) := \inf_{u \in \mathcal{C}_{v,w}} \{F_1(v) + F_2(w)\},$$

We propose an additive and an IC model. Note that an additive model was used for denoising and inpainting in [7, 18].

1. Additive Coupling:

$$\begin{aligned} E_{\text{Add}}^{\text{int}}(u) &:= \frac{1}{2} \mathbf{dist}^2(f, u) \\ &\quad + \alpha(\beta \text{TV}(u) + (1 - \beta) \text{TV}_2^{\text{int}}(u)) \end{aligned} \tag{15}$$

2. Infimal Convolution:

$$E_{\text{IC}}^{\text{int}}(u) := \frac{1}{2} \mathbf{dist}^2(f, u) + \alpha(\beta \text{TV} \square_m (1 - \beta) \text{TV}_2^{\text{int}})(u).$$

More precisely, we are interested in minimizing the slightly different functional

$$\begin{aligned} \mathcal{E}_{\text{IC}}^{\text{int}}(v, w) &= \frac{1}{2} \sum_{\mathbf{x} \in \mathcal{G}} \text{dist}^2(\gamma_{v, \widehat{w}}(\frac{1}{2}), f_{\mathbf{x}}) \\ &\quad + \alpha(\beta \text{TV}(v) + (1 - \beta) \text{TV}_2^{\text{int}}(w)) \end{aligned} \tag{16}$$

$$\begin{aligned} &= \frac{1}{2} \sum_{p \in \mathcal{G}} d_2^2(v_p, f_p, w_p) \\ &\quad + \alpha(\beta \text{TV}(v) + (1 - \beta) \text{TV}_2^{\text{int}}(w)). \end{aligned} \tag{17}$$

Here, $\gamma_{v, \widehat{w}}(\frac{1}{2})$ addresses the midpoint of the geodesic having smallest distance from f , and we finally set $u := \gamma_{v, \widehat{w}}(\frac{1}{2})$.

Remark 4.4 (TGV Model)

Concerning a TGV model on (general) manifolds one could pursue the following idea: A natural way to define the discrete gradient ∇u at $\mathbf{x} \in \mathcal{G}$ would be as a vector field in the corresponding tangent spaces $(T_{u_{\mathbf{x}}} \mathcal{M})^2$,

$$(\nabla u)_{\mathbf{x}} := \begin{cases} (0, 0)^T & \text{if } x = N_1, y = N_2, \\ (\log_{u_{\mathbf{x}}} u_{\mathbf{x}+(1,0)}, 0)^T & \text{if } x < N_1, y = N_2, \\ (0, \log_{u_{\mathbf{x}}} u_{\mathbf{x}+(0,1)})^T & \text{if } x = N_1, y < N_2, \\ \begin{pmatrix} \log_{u_{\mathbf{x}}} u_{\mathbf{x}+(1,0)} \\ \log_{u_{\mathbf{x}}} u_{\mathbf{x}+(0,1)} \end{pmatrix} & \text{otherwise,} \end{cases}$$

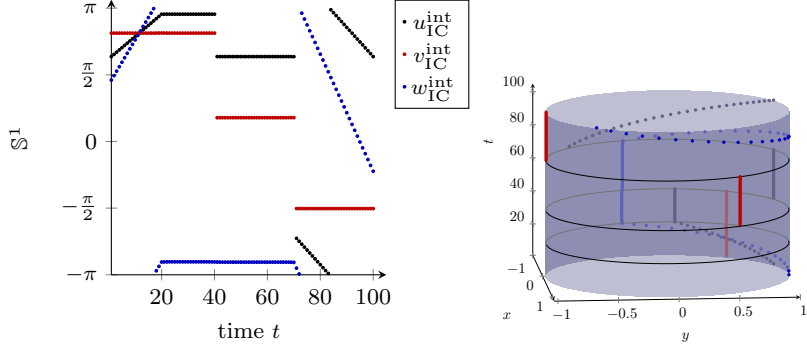


Figure 5 Decomposition of the \mathbb{S}^1 -valued signal $f = u_{IC}^{int}$ from Fig. 1 by the intrinsic midpoint IC approach (17) ($\alpha = 0.005$, $\beta = \frac{2}{5}$). Left: Original piecewise geodesic signal u_{IC}^{int} (black) determined by its angles in $[-\pi, \pi]$, and the piecewise constant component v (red) and piecewise geodesic component w_{IC}^{int} (blue), which has twice the slope compared to u_{IC}^{int} . Right: Result of the intrinsic mid point IC model in the embedding space \mathbb{R}^2 .

where $\log_p : \mathcal{M} \rightarrow T_p \mathcal{M}$ denotes the logarithmic map. For a vector field $a = (a_{\mathbf{x}})_{\mathbf{x} \in \mathcal{G}}$, $a_{\mathbf{x}} \in (T_{u_{\mathbf{x}}} \mathcal{M})^2$ the distance between a and ∇u is given by

$$\|\nabla u - a\|_u = \sum_{\mathbf{x} \in \mathcal{G}} \|(\nabla u)_{\mathbf{x}} - a_{\mathbf{x}}\|_{u_{\mathbf{x}}}.$$

However, the treatment of $\tilde{\nabla}a$ in the second summand of the TGV functional requires employing parallel transport. Then, in our algorithm, we need the derivative of the parallel transport which we have not computed so far. One way would be, to model the parallel transport by Schild's ladder.

Example 4.5 We compare the mid point IC model to the previous models by again considering the phase-valued signal $f = u_{IC}^{int}$ from Example 3.1. In Fig. 5 we see both the representation as angles in $[-\pi, \pi]$ (top plot) and the signal u_{IC}^{int} in the embedding (bottom). Its decomposition into a piecewise constant part v_{IC}^{int} and a piecewise geodesic part feature w_{IC}^{int} two apparent differences to the Lie group approach from Example 4.1: while v_{IC}^{int} possesses the same constant intervals as in the Lie IC model, its values are different. A direct comparison between the IC models does not make sense, since the decomposition is not uniquely determined, as $c(v_{IC}^{int}, w_{IC}^{int})$ here and $v_{IC}^{Lie} \circ w_{IC}^{Lie}$ in the Lie approach have to equal u_{IC}^{int} and u_{IC}^{Lie} , respectively. Hence both v and w in these models are not necessarily uniquely determined. However, the main difference is the increase and decay rate of the piecewise geodesic parts at the beginning and end of the signal, and the jump heights of the piecewise constant part. This is due to the model, where the mid point of v_{IC}^{int} and w_{IC}^{int} has to equal u_{IC}^{int} which yields twice the slope in w_{IC}^{int} compared to u_{IC}^{int} , as v_{IC}^{int} is constant. The same effect yields the doubling of the jump heights. Despite the slope and non-uniqueness, both methods have in common, that they decompose the signal u in a piecewise constant part v and a piecewise geodesic part w .

4.3. Gradient Descent Algorithm for the Intrinsic Models

In this section, we want to show how critical points of the intrinsic models can be computed by gradient descent algorithms. We restrict our attention to the intrinsic IC models (13) and (16) and the TGV model for the Lie group setting (14). For the Lie group approach we assume a bi-invariant metric. In order to compute derivatives of absolute second order differences in the IC mid-point model, we need that the manifold is in addition a symmetric space which is fulfilled in all our experiments.

For $F: \mathcal{M} \rightarrow \mathcal{M}$, we denote by $DF_p: T_p \mathcal{M} \rightarrow T_{F(p)} \mathcal{M}$ the *differential* of $F: \mathcal{M} \rightarrow \mathcal{M}$ at $p \in \mathcal{M}$ and by $\nabla_{\mathcal{M}} F$ for the Riemannian gradient of $F: \mathcal{M} \rightarrow \mathbb{R}$ which is characterized for all $\xi \in T_p \mathcal{M}$ by

$$\langle \nabla_{\mathcal{M}} F(p), \xi \rangle_p = DF_p[\xi].$$

Further, let $\exp_p: T_p \mathcal{M} \rightarrow \mathcal{M}$ be the exponential map of \mathcal{M} at p which is defined on the whole tangential space since \mathcal{M} is complete. In order to define its inverse, let $r_p \in \mathbb{R}^+$ denote the injectivity radius, i.e., the largest radius such that \exp_p is injective for all ξ with $\|\xi\|_p < r_p$, where $\|\cdot\|_p$ is the norm induced by the Riemannian metric $\langle \cdot, \cdot \rangle_p$. Then we define

$$\mathcal{D}_p := \{q \in \mathcal{M} : q = \exp_p \xi, \text{ for some } \xi \in T_p \mathcal{M} \text{ with } \|\xi\|_p < r_p\}.$$

The inverse exponential map is called the logarithmic map and denoted by $\log_p: \mathcal{D}_p \rightarrow T_p \mathcal{M}$. If the meaning is clear from the context we will use the same notation for the exponential and logarithmic map from $T_p \mathcal{M}^N$ to \mathcal{M}^N with $p \in \mathcal{M}^N$.

To apply a gradient descent algorithm we have to smooth the summands of our functionals to make them differentiable. For small $\varepsilon > 0$ we set

$$\text{TV}_\varepsilon(u) := \sum_{\mathbf{x} \in \mathcal{G}} \left(\sum_{\mathbf{y} \in \mathcal{N}_{\mathbf{x}}} \text{dist}^2(u_{\mathbf{x}}, u_{\mathbf{y}}) + \varepsilon^2 \right)^{\frac{1}{2}}, \quad (18)$$

$$\text{TV}_2^\kappa(u) := \sum_{\mathbf{x} \in \mathcal{G}} \left((d_{2,xx}^\kappa u)_{\mathbf{x}}^2 + (d_{2,yy}^\kappa u)_{\mathbf{x}}^2 + \frac{1}{2} ((d_{2,xy}^\kappa u)_{\mathbf{x}}^2 + (d_{2,yx}^\kappa u)_{\mathbf{x}}^2) + \varepsilon^2 \right)^{\frac{1}{2}},$$

$\kappa \in \{\text{Lie}, \text{int}\}$, and

$$\text{dist}_{2,1,\varepsilon}^2(a, b) = \sum_{\mathbf{x} \in \mathcal{G}} \left(\varepsilon^2 + \sum_{i=1}^d \text{dist}^2(a_{\mathbf{x},i}, b_{\mathbf{x},i}) \right)^{\frac{1}{2}}.$$

We denote the functionals with these smoothed terms accordingly by $\mathcal{E}_{\text{IC},\varepsilon}^\kappa$, $\kappa \in \{\text{Lie}, \text{int}\}$, and $\mathcal{E}_{\text{TGV},\varepsilon}^{\text{Lie}}$. The gradient descent algorithm is given in Algorithm 2.

Remark 4.6 (*Armijo condition*)

Given a differentiable function $\mathcal{E}: \mathcal{M} \rightarrow \mathbb{R}$ (or $\mathcal{E}: \mathcal{M}^N \rightarrow \mathbb{R}$) we denote the candidates for the next iterates by

$$p_l^r = \exp_{p^{(r)}}(-\rho^l s \nabla_{\mathcal{M}} \mathcal{E}(p^{(r)}))$$

Algorithm 2 Gradient Descent Algorithm for Intrinsic IC and TGV Models

Input: \mathcal{E}

Initialization: $p^{(0)}$, $s > 0$, $\rho \in (0, 1)$

for $r = 0, \dots$ **do**

 Choose smallest $l \in \mathbb{N}$ such that Armijo condition (20) in Remark 4.6 is fulfilled and set

$$\begin{aligned} \tau_r &= \rho^l s \\ p^{(r+1)} &= \exp_{v^{(r)}}(-\tau_r \nabla_{\mathcal{M}, v} \mathcal{E}(p^{(r)})). \end{aligned} \quad (19)$$

Then we choose the smallest $l \in \mathbb{N}$ such that

$$\mathcal{E}(p^{(r)}) - c\rho^l \|\nabla_{\mathcal{M}} \mathcal{E}(p^{(r)})\|^2 > \mathcal{E}(p_l^r) \quad (20)$$

with $c \in (0, 1)$. Denoting this smallest l by l^* we obtain a step size of the gradient descent algorithm for the r th step by $\tau_r = \rho^{l^*} s$, which can be used in the gradient descent (19).

Proposition 4.7 For the functionals $\mathcal{E}_{\text{IC}, \varepsilon}^{\text{Lie}}$, $\mathcal{E}_{\text{TGV}, \varepsilon}^{\text{Lie}}$, and $\mathcal{E}_{\text{IC}, \varepsilon}^{\text{int}}$, the sequence $(p^{(r)})_{r \in \mathbb{N}}$ generated by Algorithm 2 converges to a critical point.

The proof follows by [1, Proposition 4.2].

To obtain the gradients in Algorithm 2 we need to compute the gradients of all the involved summands by applying the chain rule. Using

$$\nabla_{\mathcal{M}} \text{dist}^2(\cdot, q)(p) = -2 \log_p q \quad (21)$$

we derive their explicit expression in the following.

Summands in the data fitting term.

Lie group IC: The gradient of the data term $\frac{1}{2} \text{dist}^2(f, v \circ w)$ with respect to $v_{\mathbf{x}}$ is given by

$$\begin{aligned} \nabla_{\mathcal{M}, v_{\mathbf{x}}} \left(\frac{1}{2} \text{dist}^2(f, \cdot \circ w) \right) (v) &= \nabla_{\mathcal{M}, v_{\mathbf{x}}} \left(\frac{1}{2} \text{dist}^2(f \circ w^{-1}, \cdot) \right) (v) \\ &= -\log_{v_{\mathbf{x}}} (f_{\mathbf{x}} \circ w_{\mathbf{x}}^{-1}), \end{aligned}$$

where we used the right invariance of the geodesic distance. For the gradient with respect to $w_{\mathbf{x}}$ we apply the left invariance of the metric to obtain

$$\begin{aligned} \nabla_{\mathcal{M}, w_{\mathbf{x}}} \left(\frac{1}{2} \text{dist}^2(f, v \circ \cdot) \right) (w) &= \nabla_{\mathcal{M}, v_{\mathbf{x}}} \left(\frac{1}{2} \text{dist}^2(v^{-1} \circ f, \cdot) \right) (w) \\ &= -\log_{w_{\mathbf{x}}} (v_{\mathbf{x}}^{-1} \circ f_{\mathbf{x}}). \end{aligned}$$

Lie group TGV: In this model the data term is $\frac{1}{2} \text{dist}^2$ and the derivative is given by

$$\nabla_{\mathcal{M}, u_{\mathbf{x}}} \left(\frac{1}{2} \text{dist}^2(\cdot, f) \right) (u) = -\log_{u_{\mathbf{x}}} f_{\mathbf{x}}.$$

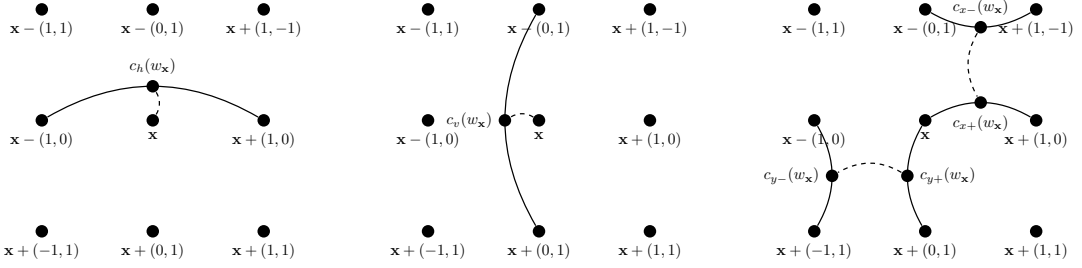


Figure 6 Schematic drawing of the mid points involved in TV_2^{int} for one \mathbf{x} . Left to right: midpoints involved in $d_{2,xx}^{\text{int}}$, $d_{2,yy}^{\text{int}}$, $d_{2,yx}^{\text{int}}$ and $d_{2,xy}^{\text{int}}$.

Mid point IC: Let $\gamma_{\widehat{x,z}}(t)$ be the geodesic whose midpoint $c(x, z) := \gamma_{\widehat{x,z}}(\frac{1}{2})$ has smallest distance to f . Then we obtain for $d_2^2(x, f, z) = \text{dist}^2(c(x, z), f)$ by the chain rule

$$\nabla_{\mathcal{M}} d_2^2(\cdot, f, z)(x) := \sum_{j=1}^d \left\langle -2 \log_{c(x,z)} f, D_x c(\cdot, z)[\Xi_j(\frac{1}{2})] \right\rangle_{c(x,z)} \Xi_j(0)$$

and similarly for z . Here $\{\Xi_1(0), \dots, \Xi_d(0)\}$ denotes an orthonormal basis of $T_x \mathcal{M}$, $\{\Xi_1(t), \dots, \Xi_d(t)\}$ its parallel transport along $\gamma_{\widehat{x,z}}(t)$, and $D_x c(\cdot, z)$ is the derivative of $c(\cdot, z)$ in x whose derivation is given in detail in [7]. Then the gradients of the data term are given by

$$\begin{aligned} \nabla_{\mathcal{M}, v_x} \left(\text{dist}^2(\gamma_{\widehat{x,z}}(\frac{1}{2}), f_x) \right) (v) &= \nabla_{\mathcal{M}} d_2^2(\cdot, f_x, w_x)(v_x), \\ \nabla_{\mathcal{M}, w_x} \left(\text{dist}^2(\gamma_{\widehat{x,z}}(\frac{1}{2}), f_x) \right) (w) &= \nabla_{\mathcal{M}} d_2^2(\cdot, f_x, v_x)(w_x). \end{aligned}$$

Summands in TV_ε . The first order difference term TV_ε is the same for both intrinsic IC models. So the gradient can be used for both minimizations.

Let $\mathbf{x} \in \mathcal{G}$, then we have for all $\mathbf{y} \in \mathcal{G}$ such that $\mathbf{x} \in \mathcal{N}_\mathbf{y}$,

$$\begin{aligned} \nabla_{\mathcal{M}, v_x} \left(\sqrt{\sum_{\mathbf{z} \in \mathcal{N}_x} \text{dist}^2(\cdot, v_{\mathbf{z}}) + \varepsilon^2} \right) (v_x) &= \sum_{\mathbf{z} \in \mathcal{N}_x} \frac{-\log_{v_x} v_{\mathbf{z}}}{\sqrt{\sum_{\mathbf{z} \in \mathcal{N}_x} \text{dist}^2(v_x, v_{\mathbf{z}}) + \varepsilon^2}} \\ \nabla_{\mathcal{M}, v_x} \left(\sqrt{\sum_{\mathbf{z} \in \mathcal{N}_y} \text{dist}^2(v_y, v_{\mathbf{z}}) + \varepsilon^2} \right) (v_x) &= \frac{-\log_{v_x} v_y}{\sqrt{\sum_{\mathbf{z} \in \mathcal{N}_y} \text{dist}^2(v_y, v_{\mathbf{z}}) + \varepsilon^2}}. \end{aligned}$$

Summands in $TV_{2,\varepsilon}$.

Lie group IC: In the computation of the gradient of $TV_{2,\varepsilon}^{\text{Lie}}$ the chain rule is an important tool. We start by the computation of the inner gradients, i.e., the gradients of $(d_{2,xx}^{\text{Lie}} w)_x^2$, $(d_{2,yy}^{\text{Lie}} w)_x^2$, $(d_{2,yx}^{\text{Lie}} w)_x^2$, and $(d_{2,xy}^{\text{Lie}} w)_x^2$.

The same technique as for the data term is used, i.e., isolation of the argument of

derivation on one side of the distance function using the bi-invariance of the metric, e.g.,

$$\nabla_{\mathcal{M}, w_{\mathbf{x}}} (d_{2,xy}^{\text{Lie}} w)^2_{\mathbf{x}}(w_{\mathbf{x}}) = -2 \log_{w_{\mathbf{x}}} (u_{\mathbf{x}-(0,1)} \circ u_{\mathbf{x}+(1,-1)}^{-1} \circ u_{\mathbf{x}+(1,0)}),$$

for more details see Appendix A. Similarly the gradients with respect to $v_{\mathbf{y}}$ can be handled, only calculating the gradient of $(d_{2,xx}^{\text{Lie}} w)^2_{\mathbf{x}}$ and $(d_{2,yy}^{\text{Lie}} w)^2_{\mathbf{x}}$ with respect to $w_{\mathbf{x}}$ is more involved. We obtain

$$\begin{aligned} \left\langle \nabla_{\mathcal{M}, w_{\mathbf{x}}} (d_{2,xx}^{\text{Lie}} w)^2_{\mathbf{x}}(w_{\mathbf{x}}), \xi \right\rangle_{w_{\mathbf{x}}} &= -2 \left\langle DL_{w_{\mathbf{x}-(1,0)} \circ w_{\mathbf{x}}^{-1}} \log_{w_{\mathbf{x}} \circ w_{\mathbf{x}-(1,0)}^{-1} \circ w_{\mathbf{x}}} w_{\mathbf{x}+(1,0)} \right. \\ &\quad \left. + DR_{w_{\mathbf{x}} \circ w_{\mathbf{x}-(1,0)}} \log_{w_{\mathbf{x}} \circ w_{\mathbf{x}-(1,0)}^{-1} \circ w_{\mathbf{x}}} w_{\mathbf{x}+(1,0)}, \xi \right\rangle_{w_{\mathbf{x}}}, \end{aligned}$$

for more details see Appendix A. The derivation of the gradient of $(d_{2,yy}^{\text{Lie}} w)^2_{\mathbf{x}}$ is analog. Finally we derive the gradient of $(\text{TV}_{2,\varepsilon}^{\text{Lie}})_{\mathbf{x}}$ as

$$\begin{aligned} \nabla_{\mathcal{M}, w_{\mathbf{x}}} ((\text{TV}_{2,\varepsilon}^{\text{Lie}})_{\mathbf{x}})(w_{\mathbf{x}}) &= \frac{1}{(\text{TV}_{2,\varepsilon}^{\text{Lie}})_{\mathbf{x}}} \times \left(\nabla_{\mathcal{M}, w_{\mathbf{x}}} (d_{2,xx}^{\text{Lie}} w)^2_{\mathbf{x}}(w_{\mathbf{x}}) + \nabla_{\mathcal{M}, w_{\mathbf{x}}} (d_{2,yy}^{\text{Lie}} w)^2_{\mathbf{x}}(w_{\mathbf{x}}) \right. \\ &\quad \left. + \frac{1}{2} \nabla_{\mathcal{M}, w_{\mathbf{x}}} (d_{2,xy}^{\text{Lie}} w)^2_{\mathbf{x}}(w_{\mathbf{x}}) + \frac{1}{2} \nabla_{\mathcal{M}, w_{\mathbf{x}}} (d_{2,yx}^{\text{Lie}} w)^2_{\mathbf{x}}(w_{\mathbf{x}}) \right). \end{aligned}$$

The element $w_{\mathbf{x}}$ appears also in $(\text{TV}_{2,\varepsilon}^{\text{Lie}})_{\mathbf{y}}$, \mathbf{y} adjacent to \mathbf{x} . The calculation of such gradients is achieved by using the chain rule and the isolation technique.

Mid point IC: In the computation of the gradient of $\text{TV}_{2,\varepsilon}^{\text{int}}$ several midpoints are involved. To avoid confusion they are shown in Fig. 6. Each $c(w_{\mathbf{x}})$ is defined as the mid point of the pixel values it connects, e.g., $c_h(w_{\mathbf{x}})$ is the mid point of $w_{\mathbf{x}-(1,0)}$ and $w_{\mathbf{x}-(0,1)}$. Note that the second order mixed terms can be written with the second order difference, e.g.,

$$\begin{aligned} (d_{2,xy}^{\text{int}} w)_{\mathbf{x}} &= \text{dist}^2(c_{x+}(w_{\mathbf{x}}), c_{x-}(w_{\mathbf{x}})) \\ &= d_2^2(w_{\mathbf{x}}, c_{x-}(w_{\mathbf{x}}), w_{\mathbf{x}+(1,0)}). \end{aligned}$$

For the summand of $\text{TV}_{2,\varepsilon}^{\text{int}}$ associated with \mathbf{x} , i.e.,

$$(\text{TV}_{2,\varepsilon}^{\text{int}})_{\mathbf{x}} := \left((d_{2,xx}^{\text{int}} w)^2_{\mathbf{x}} + (d_{2,yy}^{\text{int}} w)^2_{\mathbf{x}} + \frac{1}{2} ((d_{2,xy}^{\text{int}} w)^2_{\mathbf{x}} + (d_{2,yx}^{\text{int}} w)^2_{\mathbf{x}}) + \varepsilon^2 \right)^{\frac{1}{2}},$$

the gradient is computed using the chain rule

$$\begin{aligned} \nabla_{w_{\mathbf{x}}} (\text{TV}_{2,\varepsilon}^{\text{int}})_{\mathbf{x}} &= \frac{-1}{(\text{TV}_{2,\varepsilon}^{\text{int}})_{\mathbf{x}}(w_{\mathbf{x}})} \times \left(\log_{w_{\mathbf{x}}} c_h(w_{\mathbf{x}}) + \log_{w_{\mathbf{x}}} c_v(w_{\mathbf{x}}) \right. \\ &\quad \left. + \frac{1}{2} \nabla_{\mathcal{M}} d_2^2(\cdot, c_{x-}(w_{\mathbf{x}}), w_{\mathbf{x}+(1,0)})(w_{\mathbf{x}}) \right. \\ &\quad \left. + \frac{1}{2} \nabla_{\mathcal{M}} d_2^2(\cdot, c_{y-}(w_{\mathbf{x}}), w_{\mathbf{x}+(0,1)})(w_{\mathbf{x}}) \right). \end{aligned}$$

Furthermore $w_{\mathbf{x}}$ might occur as an element in different midpoints of $(\text{TV}_{2,\varepsilon}^{\text{int}})_{\mathbf{y}}$, for an adjacent grid point \mathbf{y} of \mathbf{x} . Rewriting all these terms as second order differences d_2 , we use the same techniques as before to compute the gradient of these components.

Summands related to TGV. The summands in the TGV model on Lie groups have a similar structure as in the IC model, which is even simpler, as no argument exists twice in one distance term. Therefore the gradients can be calculated by isolating the arguments of interest on one side of the of the distance function and then apply the chain rule with (21).

5. Numerical examples

While the gradient descent algorithm and the ADMM are implemented in MATLAB 2016b, the basic manifold functions, like logarithmic and exponential maps, as well as the distance function are implemented as C++ functions in the „Manifold-valued Image Restoration Toolbox“ (MVIRT)¹ and imported into MATLAB using mex-interfaces with the GCC 4.8.4 compiler. As a quality measure we use the mean squared error (MSE) defined by

$$\epsilon := \frac{1}{|\mathcal{G}|} \sum_{\mathbf{x} \in \mathcal{G}} \text{dist}^2(u_{\mathbf{x}}, u_{0,\mathbf{x}}),$$

where u_0 denotes the original image.

5.1. \mathbb{S}^1 -valued data

We start with the \mathbb{S}^1 -valued image in Fig. 7 from [15]. Adding wrapped Gaussian noise results in a corrupted image which we want to denoise. The model with the additive coupling of the TV and TV_2 leads to a result which does not recover the linear part very well and the edges of the boxes are smoothed. Using the TGV model we get a better reconstruction, where the linear parts in the ellipsoid and the edges of the boxes are reconstructed very well. We also obtain a lower error with the TGV model. Compared to the nonlocal methods [37] and [16] we obtain the same error, but we are only using local information of the image. Looking at the paraboloid, TGV model even outperforms the nonlocal methods visually.

5.2. \mathbb{S}^2 -valued data

Let \mathcal{M} be the two-dimensional sphere. In Fig. 8 we see a signal along three geodesics being great arcs from the north pole to the equator, along the equator, and further to the south pole. The segments are shortened by $\frac{1}{5}$, $\frac{3}{20}$, and $\frac{1}{5}$ of a circle, respectively. Hence we obtain three geodesic segments with jumps in between, see Fig. 8 (left). We apply the IC model (18) with $\alpha = \frac{11}{100}$, $\beta = \frac{1}{11}$. The result u approximates f and its decomposition into v and w yields signals that are nearly piecewise constant and piecewise geodesic, respectively, and $u = c(v, w)$.

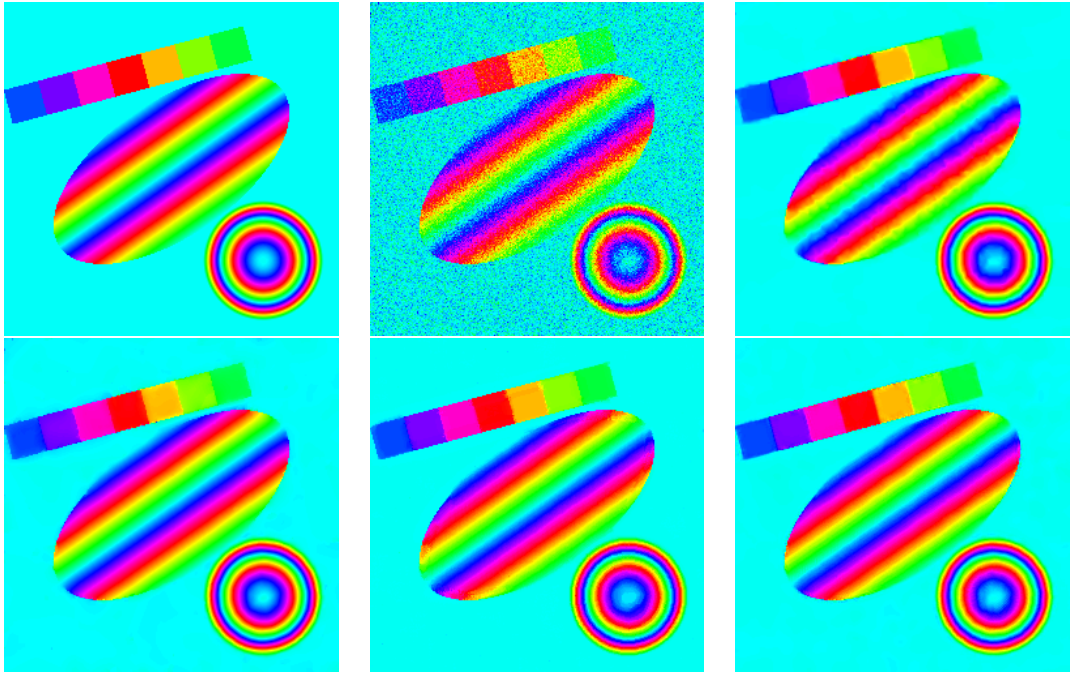


Figure 7 Denoising of an artificial S^1 image with different methods. From left to right: Original image, noisy image ($\epsilon = 88.5 \times 10^{-3}$), denoising with an additive coupling of first and second order differences [15] ($\epsilon = 5.2 \times 10^{-3}$), the TGV result ($\alpha = 1, \beta = \frac{1}{3}, \epsilon = 10^{-6}, \epsilon = 2.5 \times 10^{-3}$), the result using a graph Laplacian [16] ($\epsilon = 2.6 \times 10^{-3}$), the NL-MMSE result [37] ($\epsilon = 2.5 \times 10^{-3}$).

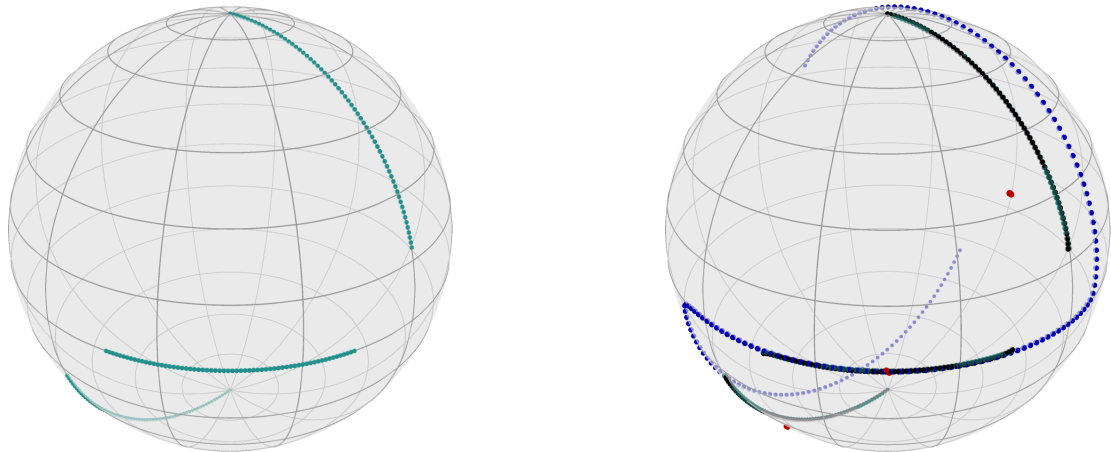


Figure 8 Decomposition of a signal f of 192 samples (left) into two parts: a part v (red) consisting of three nearly constant parts (small TV value) and a nearly piecewise geodesic curve (small TV_2 value) part w (blue). The mid point signal u (black) nearly reconstructs f (green).

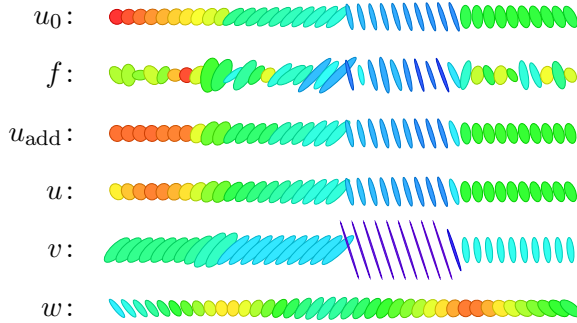


Figure 9 Denoising of a $\mathcal{P}(2)$ valued signal f . Additive coupling of TV and TV_2 in (15) leads to u_{add} . The reconstruction with the intrinsic IC model yields $u = c(v, w)$ with piecewise constant part v and geodesic part w .

5.3. SPD-valued data

Fig. 9 shows results for denoising a signal with values on the manifold of positive definite 2×2 matrices. We created a signal u_0 as the midpoint of a signal with four constant parts and one with two geodesic parts. We apply the additive model (15) and the IC model (18) to a noisy version f of this signal. The results are optimized with respect to the MSE. The parameters $\alpha\beta$ and $\alpha(1 - \beta)$ are chosen by a grid search, for the additive model on $\{0, \frac{1}{100}, \dots, 1\}$. For the IC model $\alpha\beta$ is optimized on $\{\frac{1}{10}, \frac{2}{10}, \dots, 1\}$, and $\alpha(1 - \beta)$ on $\{\frac{1}{2}, 1, \dots, 5\}$. The reconstruction from the IC model u with parameters $\alpha = 4.5, \beta = \frac{1}{9}$ yields an error of $\epsilon = 0.0269$, while the additive model u_{add} with $\alpha = 0.46$ and $\beta = 1$ has a larger error $\epsilon = 0.0316$. Also visually the result of the IC model is better, in particular the smooth parts. Looking at the components v and w , we see the decomposition into a piecewise constant and a geodesic component.

In Fig. 10 left we consider an artificial image of $\mathcal{M} = \mathcal{P}(3)$ valued data, which was used in [13]. The data are corrupted by Gaussian noise, see [37], $\sigma = 0.1$ and have the MSE of 0.0583. Denoising with the mid point model (17), $\alpha = \frac{1}{2}, \beta = \frac{1}{4}$, leads to the denoised image u in Fig. 10, middle, yielding an MSE of 0.0073. The components of the IC model show nicely the piecewise constant part v (fourth image) containing the jump and the geodesic part w (last image).

5.4. $\text{SO}(3)$ -valued data

EBSD aims at an analysis of the crystal structure of crystalline materials, see [2]. It is a fundamental task in material science since the microscopic structure affects macroscopic attributes of materials such as ductility, electrical and lifetime properties. EBSD provides for each position on the surface of a specimen a so-called Kikuchi pattern, which allows the identification of the orientation of the crystal ($\text{SO}(3)$ value). Since the crystal lattice

¹open source, available at www.mathematik.uni-kl.de/imagepro/members/bergmann/mvirt/

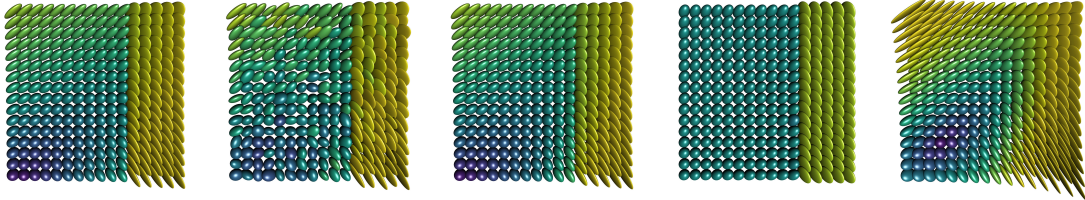


Figure 10 From Left to right: Original data f_0 , noisy measurements f , where the noise is Gaussian noise $\sigma = 0.1$, and the MSE is 0.0583, reconstruction u of the mid point IC model, $\alpha = \frac{1}{2}, \beta = \frac{1}{4}$, MSE 0.0073, consisting of the piecewise constant part v , and the geodesic part w .

possesses certain symmetries, it is invariant under its specific finite symmetry group $S \subset \text{SO}(3)$, i.e., the orientation at each grid point $i \in \mathcal{G}$ is only given as an equivalence class

$$[f_i] = \{f_i s \mid s \in S\} \in \text{SO}(3)/S, \quad f_i \in \text{SO}(3).$$

EBSD images usually consist of regions with similar orientations called grains. Fig. 11 displays a typical EBSD image of a Magnesium specimen from the software package MTEX [8]. This software package is also used for handling and color visualizing the data.

For certain macroscopic properties the pattern of orientations within single grains is important, see e.g., [9, 50]. EBSD images are often corrupted by noise so that denoising techniques have to be applied [35]. Fig. 12 displays a single grain. Since the rotations vary little within a single grain, we treat the data as $\text{SO}(3)$ -valued and apply a stretched colorization in Fig. 11 (right). Within this single grain there also occurs an edge, a so-called subgrain boundary. Thus, when denoising such kind of data, it is necessary to smooth out the noise and at the same time preserve subgrain boundaries. This gives rise to using our proposed IC model. Fig. 12 shows the results for the extrinsic and intrinsic model. For this example we restrict the pixel grid \mathcal{G} to the pixels that belong to the grain. Since within a single grain the range of orientations is rather small, we neglect the symmetries and treat the data as $\text{SO}(3)$ -valued. Both methods show good denoising results, since the data varies very little so that the difference due to the embedding is small. Nevertheless, the intrinsic approach illustrates the components better.

In Fig. 13 we compare the performance of the extrinsic TGV model with the intrinsic TGV model using the group action. The grid \mathcal{G} is again restricted to the grain and the symmetries are neglected due to the fact, we only consider a single grain. We see that both methods lead to very similar results, but the intrinsic model leads to a meaningful decomposition of the gradient. In particular the gradient a_1 has a jump at the subgrain boundary.

The measuring devices not only provide us with the estimated orientation but also several quality measures, which tell us how reliable this orientation is. One example is the mean angular deviation (MAD). After matching a Kikuchi pattern to a certain material and orientation, one can simulate a pattern using this information. Usually, the simulated pattern does not exactly match the one acquired by the detector. The MAD

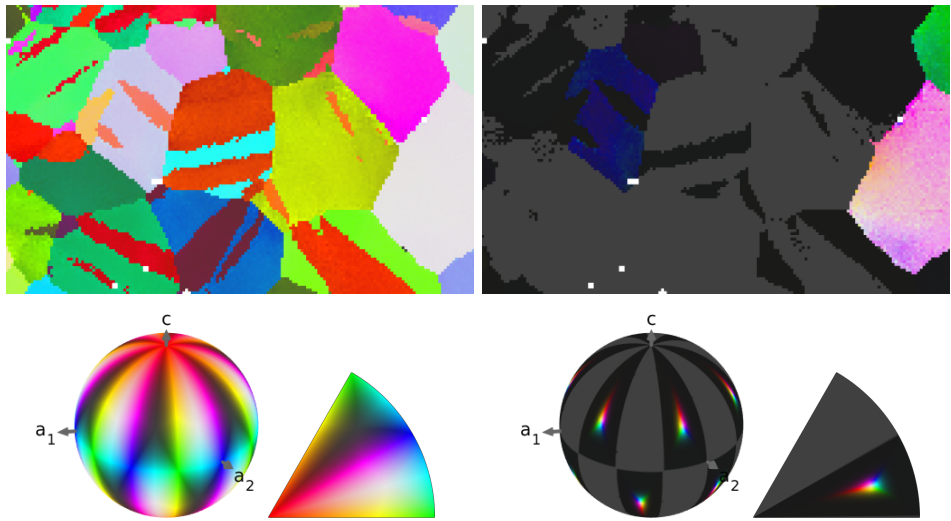


Figure 11 The raw EBSD data of a Magnesium sample, the colorization of the sphere used to assign to each rotation a certain color according to the mapping $\text{SO}(3)/S \ni m \mapsto m^{-1}(0, 0, 1)^T \in \mathbb{S}^2/S$ and the colorization of a spherical triangle. Left: standard colormap, right: stretched colormap to handle individual grains.

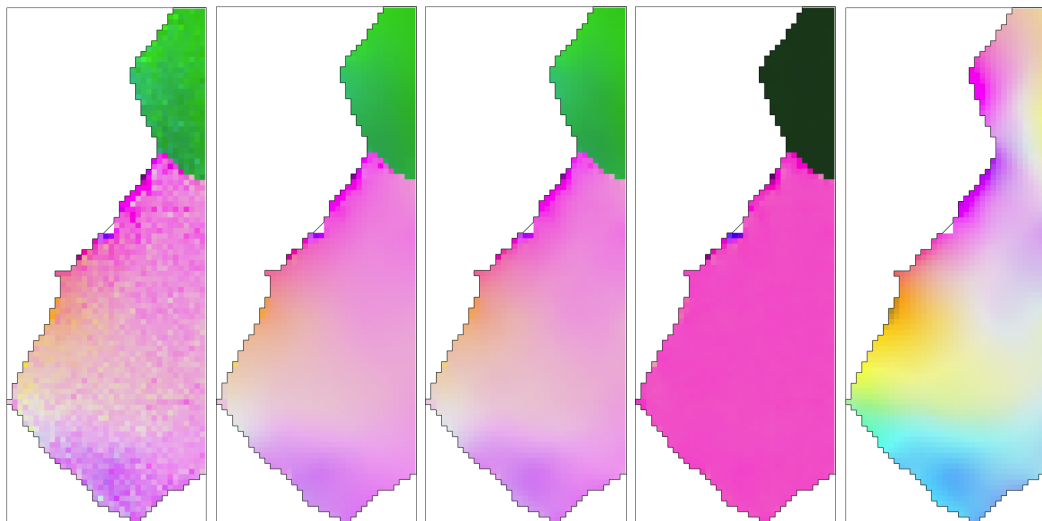


Figure 12 Denoised EBSD data of a grain with a subgrain boundary. From left to right: noisy grain, result u using the extrinsic model with embedding into \mathbb{R}^9 ($\alpha = 0.03, \beta = \frac{1}{3}$), result of the intrinsic model ($\alpha = 0.024, \beta = 0.25$), i.e., u and its two components v and w .

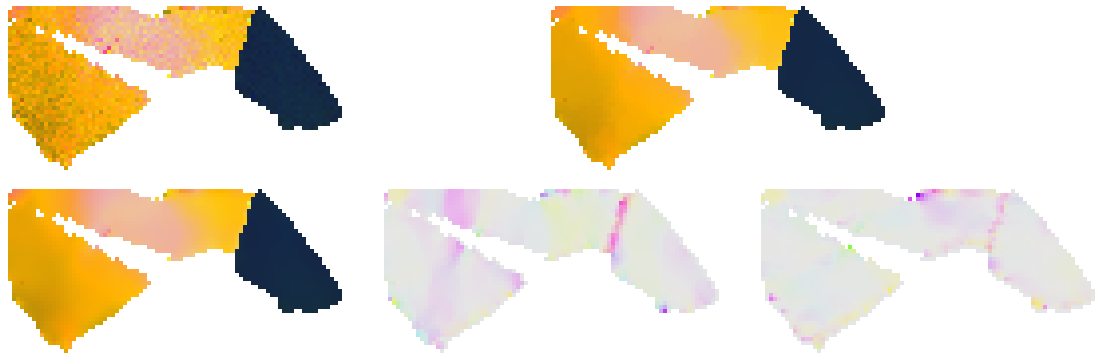


Figure 13 Denoised EBSD data of a grain with subgrain boundary. Noisy grain, result u of the extrinsic model α, β , resulting u of the intrinsic model $\alpha = 0.005, \beta = \frac{2}{3}, \epsilon = 10^{-6}$, gradient components a_1, a_2 .

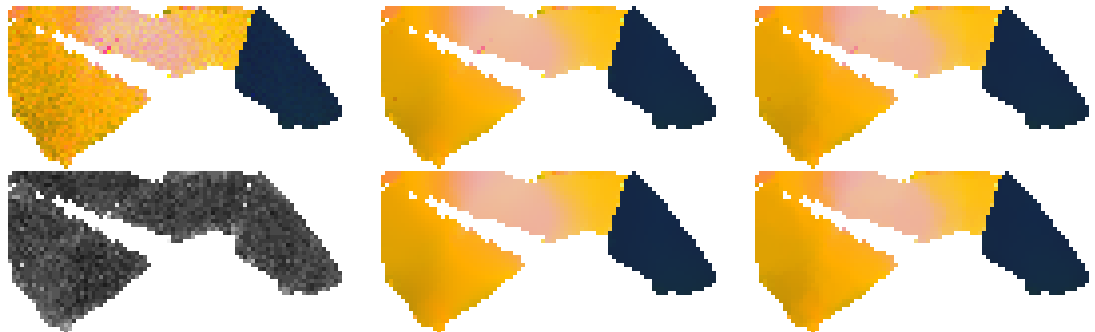


Figure 14 Denoised EBSD data of a single grain comparing the ℓ_2 -data term (top row) with the MAD weighted data term (22) (bottom row). From left to right: noisy grain, result of extrinsic IC ($\alpha = 1.2 \times 10^{-2}, \beta = \frac{1}{3}$), result of extrinsic TGV ($\alpha = 1.4 \times 10^{-2}, \beta = \frac{3}{7}$), MAD data, result with MAD weighted data term of extrinsic IC ($\alpha = 1.2 \times 10^{-2}, \beta = \frac{1}{3}$), and of extrinsic TGV ($\alpha = 1.4 \times 10^{-2}, \beta = \frac{3}{7}$).

is the mean angular deviation between the bands in these two patterns. In the next example we use the MAD to measure the reliability of the given orientation. Therefore we use a weighted data term

$$\mathcal{D}_{\text{MAD}}(u; f) = \frac{1}{2} \sum_{\mathbf{x} \in \mathcal{G}} \omega_{\mathbf{x}} \text{dist}^2(f_{\mathbf{x}}, u_{\mathbf{x}}), \quad (22)$$

with weights

$$\omega_{\mathbf{x}} = \exp(-\text{MAD}_{\mathbf{x}}) \frac{N}{\sum_{\mathbf{y} \in \mathcal{G}} \exp(-\text{MAD}_{\mathbf{y}})}$$

In Fig. 14 we show a grain and the MAD data and the regularized grain using the extrinsic models with and without the weighted data term. The results with the weighted data term have less outliers, which is advantageous. Especially considering the fact, that the computational costs are not increased by the modification of the data term and the MAD data is available from most measuring devices.

6. Conclusions

We proposed extrinsic and intrinsic variational models for the restoration of manifold-valued images, where we considered three different priors, namely additive and IC coupling of absolute values of first and second order differences and TGV. So far an intrinsic TGV approach for arbitrary manifold-valued images is an open question for future research. For Lie groups we have proposed such a model which works very good in our numerical examples. One of our future topics consists in speeding up the computation of a minimizer in the intrinsic IC models which utilize a gradient descent algorithm so far. In [13] we proposed for example a quasi-Newton method and in [7] a cyclic proximal point algorithm.

One may also think about the spatial continuous setting. For $\mathcal{M} = \mathbb{S}^1$ there exists a continuous TV approach [30, 31, 32]. For Hadamard manifolds \mathcal{M} at least the spaces $L_p(\Omega, \mathcal{M})$ were considered in the literature, see, e.g. [6] and the references therein.

A. Calculations of Gradients

In the following we give a detailed calculation of the gradient $\nabla_{\mathcal{M}, w_{\mathbf{x}}}(\text{d}_{2,xy}^{\text{Lie}} w)_{\mathbf{x}}^2(w_{\mathbf{x}})$:

$$\begin{aligned} \nabla_{\mathcal{M}, w_{\mathbf{x}}}(\text{d}_{2,xy}^{\text{Lie}} w)_{\mathbf{x}}^2(w_{\mathbf{x}}) &= \nabla_{\mathcal{M}, w_{\mathbf{x}}}(\text{dist}^2(u_{\mathbf{x}+(1,0)} \circ u_{\mathbf{x}}^{-1}, u_{\mathbf{x}+(1,-1)} \circ u_{\mathbf{x}-(0,1)}^{-1})) \\ &= \nabla_{\mathcal{M}, w_{\mathbf{x}}}(\text{dist}^2(u_{\mathbf{x}}^{-1}, u_{\mathbf{x}+(1,0)}^{-1} \circ u_{\mathbf{x}+(1,-1)} \circ u_{\mathbf{x}-(0,1)}^{-1})) \\ &= \nabla_{\mathcal{M}, w_{\mathbf{x}}}(\text{dist}^2(u_{\mathbf{x}}, u_{\mathbf{x}-(0,1)} \circ u_{\mathbf{x}+(1,-1)}^{-1} \circ u_{\mathbf{x}+(1,0)})) \\ &= -2 \log_{w_{\mathbf{x}}}(u_{\mathbf{x}-(0,1)} \circ u_{\mathbf{x}+(1,-1)}^{-1} \circ u_{\mathbf{x}+(1,0)}), \end{aligned}$$

here we also used that a bi-invariant metric is invariant to inversion, i.e., $d(p, q) = d(p^{-1}, q^{-1})$ for $p, q \in \mathcal{M}$.

In the following we give a detailed calculation of the gradient $\nabla_{\mathcal{M}, w_{\mathbf{x}}} (\mathrm{d}_{2,xx}^{\mathrm{Lie}} w)_{\mathbf{x}}^2(w_{\mathbf{x}})$: We use the definition of the gradient and for $\xi \in T_{w_{\mathbf{x}}} \mathcal{M}$ we obtain

$$\begin{aligned}
& \left\langle \nabla_{\mathcal{M}, w_{\mathbf{x}}} (\mathrm{d}_{2,xx}^{\mathrm{Lie}} w)_{\mathbf{x}}^2(w_{\mathbf{x}}), \xi \right\rangle_{w_{\mathbf{x}}} \\
&= \left\langle \nabla_{\mathcal{M}, w_{\mathbf{x}}} (\mathrm{dist}^2(\cdot \circ w_{\mathbf{x}-(1,0)}^{-1} \circ \cdot, w_{\mathbf{x}+(1,0)})) (w_{\mathbf{x}}), \xi \right\rangle_{w_{\mathbf{x}}} \\
&= D(\mathrm{dist}^2(\cdot \circ w_{\mathbf{x}-(1,0)}^{-1} \circ \cdot, w_{\mathbf{x}+(1,0)}))_{w_{\mathbf{x}}}[\xi] \\
&= D(\mathrm{dist}^2(\cdot, w_{\mathbf{x}+(1,0)}))_{w_{\mathbf{x}} \circ w_{\mathbf{x}-(1,0)}^{-1} \circ w_{\mathbf{x}}} [D(w_{\mathbf{x}} \circ w_{\mathbf{x}-(1,0)}^{-1} \circ w_{\mathbf{x}})_{w_{\mathbf{x}}}[\xi]] \\
&= -2 \left\langle \log_{w_{\mathbf{x}} \circ w_{\mathbf{x}-(1,0)}^{-1} \circ w_{\mathbf{x}}} w_{\mathbf{x}+(1,0)}, D(\cdot \circ w_{\mathbf{x}-(1,0)}^{-1} \circ \cdot)_{w_{\mathbf{x}}}[\xi] \right\rangle_{w_{\mathbf{x}} \circ w_{\mathbf{x}-(1,0)}^{-1} \circ w_{\mathbf{x}}} \\
&= -2 \left\langle \log_{w_{\mathbf{x}} \circ w_{\mathbf{x}-(1,0)}^{-1} \circ w_{\mathbf{x}}} w_{\mathbf{x}+(1,0)}, DL_{w_{\mathbf{x}} \circ w_{\mathbf{x}-(1,0)}^{-1}} \xi + DR_{w_{\mathbf{x}-(1,0)}^{-1} \circ w_{\mathbf{x}}} \xi \right\rangle_{w_{\mathbf{x}} \circ w_{\mathbf{x}-(1,0)}^{-1} \circ w_{\mathbf{x}}} \\
&= -2 \left\langle DL_{w_{\mathbf{x}-(1,0)} \circ w_{\mathbf{x}}^{-1}} \log_{w_{\mathbf{x}} \circ w_{\mathbf{x}-(1,0)}^{-1} \circ w_{\mathbf{x}}} w_{\mathbf{x}+(1,0)} \right. \\
&\quad \left. + DR_{w_{\mathbf{x}}^{-1} \circ w_{\mathbf{x}-(1,0)}} \log_{w_{\mathbf{x}} \circ w_{\mathbf{x}-(1,0)}^{-1} \circ w_{\mathbf{x}}} w_{\mathbf{x}+(1,0)}, \xi \right\rangle_{w_{\mathbf{x}}}.
\end{aligned}$$

B. Special Manifolds

B.1. The d -dimensional Sphere

Let $\mathbb{S}^d = \{p \in \mathbb{R}^{d+1} : \|p\|_2 = 1\}$ denote the d -dimensional unit sphere embedded in \mathbb{R}^{d+1} . The tangential space at $p \in \mathbb{S}^d$ is given by

$$T_p \mathbb{S}^d = \{\xi \in \mathbb{R}^{d+1} : \langle p, \xi \rangle = 0\}.$$

A Riemannian metric is the metric from the embedding space, i.e., the Euclidean inner product. The geodesic distance related to this metric is given by

$$\mathrm{dist}(p, q) = \arccos \langle p, q \rangle,$$

where $\langle \cdot, \cdot \rangle$ is the standard scalar product in \mathbb{R}^{d+1} . The geodesic $\gamma_{p,\xi}(t)$ with $\gamma_{p,\xi}(0) = p$ and $\dot{\gamma}_{p,\xi}(0) = \xi$ is given by

$$\gamma_{p,\xi}(t) = \cos(t\|\xi\|_2)p + \sin(t\|\xi\|_2) \frac{\xi}{\|\xi\|_2}.$$

The exponential and logarithmic map read as

$$\begin{aligned}
\exp_p(\xi) &= p \cos(\|\xi\|) + \frac{\xi}{\|\xi\|} \sin(\|\xi\|), \\
\log_p(q) &= \mathrm{dist}_{\mathbb{S}^d}(p, q) \frac{q - \langle p, q \rangle p}{\|q - \langle p, q \rangle p\|}, \quad p \neq -q.
\end{aligned}$$

The orthogonal projection of $x \in \mathbb{R}^{d+1}$ onto \mathbb{S}^d is given by $\Pi(x) = x/\|x\|_2$.

B.2. The special orthogonal group

Let $\text{SO}(3) = \{p \in \mathbb{R}^{3,3} : p^T p = I_3, \det(p) = 1\}$, be the space of rotations in \mathbb{R}^3 . The tangent space at $p \in \text{SO}(3)$ is $T_p \text{SO}(3) = p \text{Skew}(3)$, with $\text{Skew}(3) = \{p \in \mathbb{R}^{3,3} : p^T + p = 0\}$. It is a Lie group with bi-invariant metric and geodesic distance

$$\text{dist}_{\text{SO}(3)}(p, q) = \sqrt{2} \arccos\left(\frac{\text{tr}(p^T q) - 1}{2}\right).$$

An isometric representation of the rotations in \mathbb{R}^3 is given by the unit quaternions, see [34]: for $p_1, p_2 \in \mathbb{R}^4$, $p_1 = (s_1, v_1)^T, p_2 = (s_2, v_2)^T$, $v_1, v_2 \in \mathbb{R}^3$, the multiplication is defined by

$$p \circ q = \begin{pmatrix} s_1 s_2 - v_1^T v_2 \\ s_1 v_2 + s_2 v_1 + v_1 \times v_2 \end{pmatrix},$$

the unit element is $e = (1, 0, 0, 0)^T$ and the inverse is given by

$$p^{-1} = (p_1, -p_2, -p_3, -p_4).$$

A rotation of a vector $x \in \mathbb{R}^3$ around the angle $\alpha \in (0, \pi]$ and axis $r \in \mathbb{S}^2$ can be realized with

$$p(\alpha, r) := \begin{pmatrix} \cos(\frac{\alpha}{2}) \\ \sin(\frac{\alpha}{2})r \end{pmatrix}, p(\alpha, r) \circ \begin{pmatrix} 0 \\ x \end{pmatrix} \circ p(\alpha, r)^{-1} = \text{rot}(\alpha, r).$$

Note that $p(\alpha, r) \in \mathbb{S}^3$, further $p(\alpha_1, r_1) \circ p(\alpha_2, r_2) \in \mathbb{S}^3$, so the rotations can be identified with elements on the sphere \mathbb{S}^3 . As p and $-p$ yield the same rotation, we have a bijection between $\text{SO}(3)$ and $\mathbb{S}^3/\{-1, 1\}$. Furthermore $(\text{SO}(3), \text{dist}_{\text{SO}(3)})$ is isometric to $(\mathbb{S}^3/\{-1, 1\}, \sqrt{2} \text{dist}_{\mathbb{S}^3/\{-1, 1\}})$, with

$$\text{dist}_{\mathbb{S}^3/\{-1, 1\}}(x_1, x_2) = \arccos|\langle x_1, x_2 \rangle|.$$

The exponential map, logarithmic map, and the projection on \mathbb{S}^3 can be used, with a few adjustments. The result of the exponential map and the projection is chosen, such that the first entry is positive. For the computation of the logarithmic map $\log_p q$, we chose the representation of q having the smallest distance to p .

B.3. Symmetric positive definite matrices

The dimension of the manifold $\mathcal{P}(r)$ of symmetric positive definite matrices is $d = \frac{r(r+1)}{2}$. Then the affine invariant geodesic distance is given by

$$\text{dist}_{\mathcal{P}(r)}(p, q) = \|\text{LOG}(p^{-\frac{1}{2}} q p^{-\frac{1}{2}})\|_{\text{F}},$$

where $\|\cdot\|_{\text{F}}$ denotes the Frobenius norm of matrices and EXP and LOG denote the matrix exponential and logarithm, respectively. The tangential space at $p \in \mathcal{P}(r)$ is given by

$$T_p \mathcal{P}(r) = \{p^{\frac{1}{2}} \xi p^{\frac{1}{2}} : \xi \in \text{Sym}(r)\} = \text{Sym}(r),$$

where $\text{Sym}(r)$ denotes the space of symmetric $r \times r$ matrices. The Riemannian metric reads

$$\langle \xi_1, \xi_2 \rangle_p = \text{tr}(\xi_1 p^{-1} \xi_2 p^{-1}), \quad \xi_1, \xi_2 \in T_p \mathcal{P}(r).$$

The exponential and the logarithmic map are

$$\begin{aligned} \exp_p(\xi) &= p^{\frac{1}{2}} \text{EXP}(p^{-\frac{1}{2}} \xi p^{-\frac{1}{2}}) p^{\frac{1}{2}}, \\ \log_p(q) &= p^{\frac{1}{2}} \text{LOG}(p^{-\frac{1}{2}} q p^{-\frac{1}{2}}) p^{\frac{1}{2}}. \end{aligned}$$

We embed the manifold of symmetric positive definite matrices $\mathcal{P}(r)$ into \mathbb{R}^n , $n = \frac{r(r+1)}{2}$ using the canonical embedding of the upper triangular matrix. Then the projection onto the closure of the manifold $\mathcal{P}(r)$ is given as follows: let $q = u\Lambda u^T$ denote the eigenvalue decomposition of an real-valued symmetric matrix $q \in \mathbb{R}^{r,r}$ represented as before by its upper triangular entries as a vector in \mathbb{R}^n . Hence u is an orthogonal matrix, and $\Lambda = \text{diag}(\lambda_1, \dots, \lambda_r)$ is the diagonal matrix of the eigenvalues of q . The projection is then given by

$$\Pi(q) = u\tilde{\Lambda}u^T, \quad \tilde{\Lambda} := \text{diag}(\tilde{\lambda}_1, \dots, \tilde{\lambda}_r), \quad \tilde{\lambda}_i := \max\{0, \lambda_i\}.$$

Acknowledgement. Funding by the German Research Foundation (DFG) within the project STE 571/13-1 & BE 5888/2-1 and within the Research Training Group 1932, project area P3, is gratefully acknowledged. Furthermore, G. Steidl acknowledges the support by the German Federal Ministry of Education and Research (BMBF) through grant 05M13UKA (AniS).

References

- [1] P.-A. Absil, R. Mahony, and R. Sepulchre. *Optimization Algorithms on Matrix Manifolds*. Princeton University Press, Princeton and Oxford, 2008.
- [2] B. L. Adams, S. I. Wright, and K. Kunze. Orientation imaging: The emergence of a new microscopy. *Journal Metallurgical and Materials Transactions A*, 24:819–831, 1993.
- [3] V. Arsigny, X. Pennec, and N. Ayache. Bi-invariant means in Lie groups. application to left-invariant polyaffine transformations. *HAL Preprint*, 00071383, 2006.
- [4] H. Attouch, J. Bolte, and B. F. Svaiter. Convergence of descent methods for semi-algebraic and tame problems: proximal algorithms, forward–backward splitting, and regularized Gauss–Seidel methods. *Mathematical Programming*, 137(1):91–129, 2013.
- [5] J.-F. Aujol, G. Gilboa, T. Chan, and S. Osher. Structure-texture image decomposition—modeling, algorithms, and parameter selection. *International Journal of Computer Vision*, 67(1):111–136, 2006.

- [6] M. Bačák. *Convex analysis and optimization in Hadamard spaces*, volume 22 of *De Gruyter Series in Nonlinear Analysis and Applications*. De Gruyter, Berlin, 2014.
- [7] M. Bačák, R. Bergmann, G. Steidl, and A. Weinmann. A second order non-smooth variational model for restoring manifold-valued images. *SIAM Journal on Scientific Computing*, 38(1):A567–A597, 2016.
- [8] F. Bachmann and R. Hielscher. MTEX – MATLAB toolbox for quantitative texture analysis. <http://mtex-toolbox.github.io/>, 2005–2016.
- [9] F. Bachmann, R. Hielscher, P. E. Jupp, W. Pantleon, H. Schaeben, and E. Wegert. Inferential statistics of electron backscatter diffraction data from within individual crystalline grains. *Journal of Applied Crystallography*, 43:1338–1355, 2010.
- [10] F. Balle, T. Beck, D. Eifler, J. H. Fitschen, S. Schuff, and G. Steidl. Strain analysis by a total generalized regularization optical flow model. *ArXiv Preprint*, 1704.06028, 2017.
- [11] F. Balle, D. Eifler, J. H. Fitschen, S. Schuff, and G. Steidl. Computation and visualization of local deformation for multiphase metallic materials by infimal convolution of TV-type functionals. In *SSVM 2015*, Lecture Notes in Computer Science, pages 385–396. Springer, 2015.
- [12] R. Bamler and P. Hartl. Synthetic aperture radar interferometry. *Inverse Problems*, 14(4):R1–R54, 1998.
- [13] R. Bergmann, R. H. Chan, R. Hielscher, J. Persch, and G. Steidl. Restoration of manifold-valued images by half-quadratic minimization. *Inverse Problems and Imaging*, 10(2):281–304, 2016.
- [14] R. Bergmann, J. H. Fitschen, J. Persch, and G. Steidl. Infimal convolution coupling of first and second order differences on manifold-valued images. In F. Lauze, Y. Dong, and A. B. Dahl, editors, *Scale Space and Variational Methods in Computer Vision: 6th International Conference, SSVM 2017, Kolding, Denmark, June 4–8, 2017, Proceedings*, pages 447–459. Springer International Publishing, Cham, 2017.
- [15] R. Bergmann, F. Laus, G. Steidl, and A. Weinmann. Second order differences of cyclic data and applications in variational denoising. *SIAM Journal on Imaging Sciences*, 7(4):2916–2953, 2014.
- [16] R. Bergmann and D. Tenbrinck. A graph framework for manifold-valued data. 2017. arXiv Preprint 1702.05293.
- [17] R. Bergmann and A. Weinmann. Inpainting of cyclic data using first and second order differences. In *Energy Minimization Methods in Computer Vision and Pattern Recognition*, pages 155–168. Springer, 2015.

- [18] R. Bergmann and A. Weinmann. A second order TV-type approach for inpainting and denoising higher dimensional combined cyclic and vector space data. *Journal of Mathematical Imaging and Vision*, 55(3):401–427, 2016.
- [19] S. Boyd, N. Parikh, E. Chu, B. Peleato, and J. Eckstein. Distributed optimization and statistical learning via the alternating direction method of multipliers. *Foundations and Trends in Machine Learning*, 3(1):101–122, 2011.
- [20] K. Bredies, K. Kunisch, and T. Pock. Total generalized variation. *SIAM Journal on Imaging Sciences*, 3(3):492–526, 2010.
- [21] K. Bredies and T. Valkonen. Inverse problems with second-order total generalized variation constraints. In *International Conference on Sampling Theory and Applications*, 2011.
- [22] M. Burger, A. Sawatzky, and G. Steidl. First order algorithms in variational image processing. In R. Glowinski, S. Osher, and W. Yin, editors, *Operator Splittings and Alternating Direction Methods*. Springer, 2016.
- [23] R. Bürgmann, P. A. Rosen, and E. J. Fielding. Synthetic aperture radar interferometry to measure earth’s surface topography and its deformation. *Annu. Rev. Earth Planet. Sci.*, 28(1):169–209, 2000.
- [24] A. Chambolle and P.-L. Lions. Image recovery via total variation minimization and related problems. *Numerische Mathematik*, 76(2):167–188, 1997.
- [25] D. Cremers and E. Strekalovskiy. Total cyclic variation and generalizations. *Journal of Mathematical Imaging and Vision*, 47(3):258–277, 2013.
- [26] D. L. Donoho and G. Kutyniok. Geometric separation using a wavelet-shearlet dictionary. In *SampTA 2009*, 2009.
- [27] J. H. Fitschen. *Variational Models in Image Processing with Applications in the Materials Sciences*. Dissertation, University of Kaiserslautern, 2017. Similarly: Verlag Dr. Hut, ISBN 978-3843932455, 2017.
- [28] P. Fletcher and S. Joshi. Riemannian geometry for the statistical analysis of diffusion tensor data. *Signal Processing*, 87:250–262, 2007.
- [29] D. Gabay and B. Mercier. A dual algorithm for the solution of nonlinear variational problems via finite element approximations. *Computer and Mathematics with Applications*, 2:17–40, 1976.
- [30] M. Giaquinta, G. Modica, and J. Souček. Variational problems for maps of bounded variation with values in S^1 . *Calculus of Variation*, 1(1):87–121, 1993.
- [31] M. Giaquinta and D. Mucci. The BV-energy of maps into a manifold: relaxation and density results. *Ann. Sc. Norm. Super. Pisa Cl. Sci.*, 5(4):483–548, 2006.

- [32] M. Giaquinta and D. Mucci. Maps of bounded variation with values into a manifold: total variation and relaxed energy. *Pure and Applied Mathematics Quarterly*, 3(2):513–538, 2007.
- [33] R. Glowinski and A. Marroco. Sur l’approximation, par éléments finis d’ordre un, et la résolution, par pénalisation-dualité d’une classe de problèmes de Dirichlet non linéaires. *Revue française d’automatique, informatique, recherche opérationnelle. Analyse numérique*, 9(2):41–76, 1975.
- [34] M. Gräf. A unified approach to scattered data approximation on \mathbb{S}^3 and $\text{SO}(3)$. *Advances in Computational Mathematics*, 37(3):379–392, 2012.
- [35] V. K. Gupta and S. R. Agnew. A simple algorithm to eliminate ambiguities in ebsd orientation map visualization and analyses: Application to fatigue crack-tips/wakes in aluminum alloys. *Microscopy and Microanalysis*, 16:831, 2010.
- [36] M. Holler and K. Kunisch. On infimal convolution of TV-type functionals and applications to video and image reconstruction. *SIAM Journal on Imaging Sciences*, 7(4):2258–2300, 2014.
- [37] F. Laus, M. Nikolova, J. Persch, and G. Steidl. A nonlocal denoising algorithm for manifold-valued images using second order statistics. *SIAM Journal on Imaging Sciences*, 10(1):416–448, March 2017.
- [38] J. Lellmann, E. Strekalovskiy, S. Koetter, and D. Cremers. Total variation regularization for functions with values in a manifold. In *IEEE ICCV 2013*, pages 2944–2951, 2013.
- [39] J. Nash. The imbedding problem for Riemannian manifolds. *Annals of Mathematics*, 63(1):20–63, 1956.
- [40] K. Papafitsoros and C. B. Schönlieb. A combined first and second order variational approach for image reconstruction. *Journal of Mathematical Imaging and Vision*, 2(48):308–338, 2014.
- [41] R. T. Rockafellar. *Convex Analysis*. Princeton University Press, 1970.
- [42] G. Rosman, X.-C. Tai, R. Kimmel, and A. M. Bruckstein. Augmented-Lagrangian regularization of matrix-valued maps. *Methods and Applications of Analysis*, 21(1):121–138, 2014.
- [43] G. Rosman, Y. Wang, X.-C. Tai, R. Kimmel, and A. M. Bruckstein. Fast regularization of matrix-valued images. In *Efficient Algorithms for Global Optimization Methods in Computer Vision*, pages 19–43. Springer, 2014.
- [44] L. I. Rudin, S. Osher, and E. Fatemi. Nonlinear total variation based noise removal algorithms. *Physica D: Nonlinear Phenomena*, 60(1):259–268, 1992.

- [45] S. Setzer and G. Steidl. Variational methods with higher order derivatives in image processing. In *Approximation XII: San Antonio 2007*, pages 360–385, 2008.
- [46] S. Setzer, G. Steidl, and T. Teuber. Infimal convolution regularizations with discrete ℓ_1 -type functionals. *Communications in Mathematical Sciences*, 9(3):797–827, 2011.
- [47] J.-L. Starck, M. Elad, and D. L. Donoho. Image decomposition via the combination of sparse representations and a variational approach. *IEEE Transactions on Image Processing*, 14(10):1570–1582, 2005.
- [48] G. Steidl, S. Setzer, B. Popilka, and B. Burgeth. Restoration of matrix fields by second order cone programming. *Computing*, 81:161–178, 2007.
- [49] E. Strekalovskiy and D. Cremers. Total variation for cyclic structures: convex relaxation and efficient minimization. In *2011 IEEE Conference on Computer Vision and Pattern Recognition (CVPR)*, pages 1905–1911, 2011.
- [50] S. Sun, B. Adams, and W. King. Observation of lattice curvature near the interface of a deformed aluminium bicrystal. *Phil. Mag. A*, 80:9–25, 2000.
- [51] T. Valkonen, K. Bredies, and F. Knoll. Total generalized variation in diffusion tensor imaging. *SIAM Journal on Imaging Sciences*, 6(1):487–525, 2013.
- [52] Y. Wang, W. Yin, and J. Zeng. Global convergence of ADMM in nonconvex nonsmooth optimization. *ArXiv preprint 1511.06324*, 2015.
- [53] A. Weinmann, L. Demaret, and M. Storath. Total variation regularization for manifold-valued data. *SIAM Journal on Imaging Sciences*, 7(4):2226–2257, 2014.
- [54] H. Whitney. Differentiable manifolds. *Annals of Mathematics*, 37(3):645–680, 1936.